ACS OMEGA

Open Access

http://pubs.acs.org/journal/acsodf

Article

Polarity-Induced Morphological Transformation with Tunable Optical Output of Terpyridine−Phenanthro[9,10-*d*]imidazole-Based Ligand and Its Zn(II) Complexes with *I*−*V* Characteristics

Priya Rana, Abigail Jennifer G, Shanmuka Rao T, Sabyasachi Mukhopadhyay, Elumalai Varathan,* and Priyadip Das*

Cite This: *ACS Omega* 2023, 8, 48855−48872

Read Online

ACCESS | Metrics & More | Article Recommendations | Supporting Information

ABSTRACT: Self-assembled nanostructures obtained from various functional π-conjugated organic molecules have been able to draw substantial interest due to their inherent optical properties, which are imperative for developing optoelectronic devices, multiple-color-emitting devices with color-tunable displays, and optical sensors. These π-conjugated molecules have proven their potential employment in various organic electronic applications. Therefore, the stimuli-responsive fabrication of these π-conjugated systems into a well-ordered assembly is extremely crucial to tuning their inherent optical properties for improved performance in organic electronic applications. To this end, herein, we have designed and synthesized a functional π-conjugated molecule (**TP**) having phenanthro[9,10-*d*]imidazole with terpyridine substitution at the 2 position and its corresponding metal complexes (**TPZn** and $(\mathbf{TP})_2\mathbf{Zn}$). By varying the polarity of the self-assembly medium, **TP**, **TPZn**, and $(\mathbf{TP})_2\mathbf{Zn}$ are fabricated into well-ordered superstructures with morphological individualities. However, this medium polarity-induced self-assembly can tune the inherent optical properties of **TP**, **TPZn**, and $(\mathbf{TP})_2\mathbf{Zn}$ and generate multiple fluorescence colors. Particularly, this property makes them useful for organic electronic applications, which require adjustable luminescence output. More importantly, in 10% aqueous-THF medium, **TPZn** exhibited H-type aggregation-induced white light emission and behaved as a single-component white light emitter. The experimentally obtained results of the solvent polarity-induced variation in optical properties as well as self-assembly patterns were further confirmed by theoretical investigation using density functional theory calculations. Furthermore, we investigated the *I*−*V* characteristics, both vertical and horizontal, using ITO and glass surfaces coated with **TP**, **TPZn**, and $(\mathbf{TP})_2\mathbf{Zn}$, respectively, and displayed maximum current density for the **TPZn**-coated surface with the order of measured current density **TPZn** > **TP** > $(\mathbf{TP})_2\mathbf{Zn}$. This observed order of current density measurements was also supported by a direct band gap calculation associated with the frontier molecular orbitals using the Tauc plot. Hence, solvent polarity-induced self-assembly behavior with adjustable luminescence output and superior *I*−*V* characteristics of **TPZn** make it an exceptional candidate for organic electronic applications and electronic device fabrication.

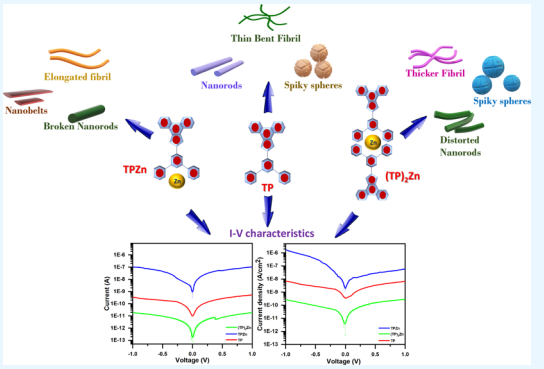

INTRODUCTION

The development of functional superstructures with morphological individualities by means of energy as well as resource-saving conventional procedures such as molecular self-assembly is an area of passionate investigation.[1−4] In many cases, the precise application of the self-assembled structures is solely controlled by the morphological identities.[5−8] Therefore, the fabrication of multiple nanostructures with various morphologies from a single molecular backbone by tuning the self-assembly parameters is of prime significance and extremely desirable.[9,10] In this context, building blocks such as low-molecular-weight organic molecules, dendrimers, π-conjugated systems, macromolecules, and organic polymers have been extensively studied during the past decade. Among them, π-conjugated systems having a suitable chromogenic moiety, including conjugated small molecules, polymers, oligomers, and carbonaceous materials, etc., are considered to be promising molecular building blocks for developing superstructures with various morphologies and switchable optical properties in response to diverse external parameters.[11−16] However, very few examples have addressed the suitable transformation from molecules to devices, and this is believed

Received: August 24, 2023
Revised: November 17, 2023
Accepted: November 29, 2023
Published: December 14, 2023

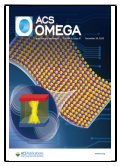

Scheme 1. Schematic Representation of the Synthesis of TP, TPZn, and $(TP)_2Zn$

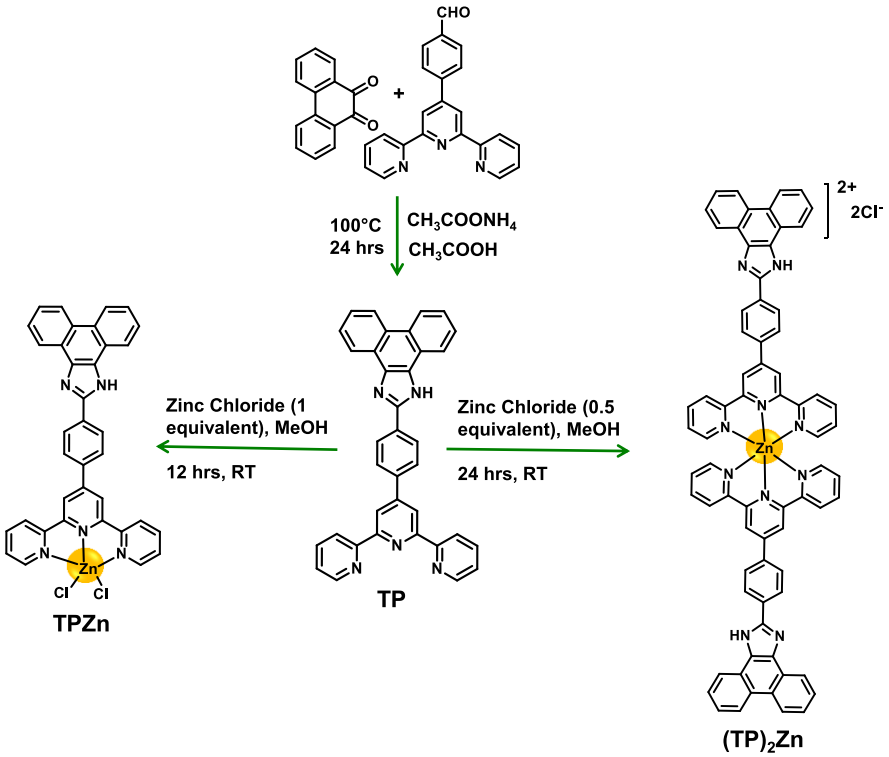

to be one of the most difficult issues. The interchain electronic coupling of a π-conjugated system will determine the performance of these π-conjugated system-based electronic devices.[12,17,18] Therefore, for a proper implication of the π-conjugated system in molecular electronics, a detailed understanding of the self-assembly and fabrication-induced optical properties is extremely crucial and becomes one of the most exciting areas of research.[11,19,20] In this context, low-molecular-weight π-conjugated organic molecules due to their ease of synthesis, ready obtainability, high purity, and unique electronic properties can be considered as an ideal component for device fabrication, for example, light modulators, light-emitting diodes, and field-effect transistors.[13,21−24] The synthetic flexibility, broad diversity, and functionality with respect to molecular structure and geometry make them superior modules compared to inorganic materials. Recently, our group described the solvent polarity-induced self-assembly and optical properties of two isomeric functional π-conjugated molecules. Upon changing the solvent polarity of the self-assembly medium, both molecules were fabricated into different supramolecular architectures with various morphologies and engendered multiple tunable fluorescence colors (blue−green−yellow−white). More significantly, both of them displayed aggregation-induced white light emission in a highly polar 90% aqueous-THF solvent medium.[12]

Supramolecular π-conjugated (semiconducting) polymers and biomolecules developed through the well-ordered organization of π-conjugated molecules in a specific supramolecular manner are considered to date the most promising components used to develop cost-effective and flexible electronic devices. These supramolecular π-conjugated polymers have been already used for the fabrication of prototype field-effect transistors (FETs),[25] light-emitting diodes (LEDs),[26,27] photovoltaic cells,[28] and related devices. On the other hand, J-aggregated organic dye molecules with superlarge red-shifted absorption facilitate the construction of supramolecular near-infrared (NIR) materials with tuned structures and improved functionalities, which have been effectively employed in different areas including biological imaging, phototherapy, solar cells, and electronic devices.[28−31] Furthermore, π-conjugated biomolecules derived from aromatic amino acids self-assemble into multifunctional biomaterials with distinct morphology as well as photoactive properties suitable for potential biomedical applications including drug delivery and phototherapy.[32] Therefore, in terms of sophisticated molecular engineering, a detailed investigation of the self-assembly properties of these low-molecular-weight π-conjugated molecules is extremely essential as they provide admirable optical, electrical, photophysical, and mechanical characteristics through molecular self-assembly.

On the other hand, metal ion-induced self-assembly of organic building blocks is a proficient technique to develop well-defined superstructures.[33] Metal−ligand interactions overcome the limitations set by the already existing noncovalent intermolecular interactions.[34,35] Therefore, suitably designed π-conjugated low-molecular-weight molecules with effective coordination sites can bind with different transition metals, which eventually alters the nature of preexisting supramolecular interactions compared to the absence of metal ions. The nature of aggregation as well as the electronic properties of the fabricated well-ordered structures originating from the metal-coordinated π-conjugated system is governed by the self-assembly properties of the building block as well as specific metal−ligand interactions.[36]

It is well-known that different derivates of phenanthro[9,10-*d*]imidazole, especially the 2-substituted ones, have been extensively used as luminescent sensors, photoactive materials, and OLED components for nonlinear optical applica-

https://doi.org/10.1021/acsomega.3c06283
ACS Omega 2023, 8, 48855−48872

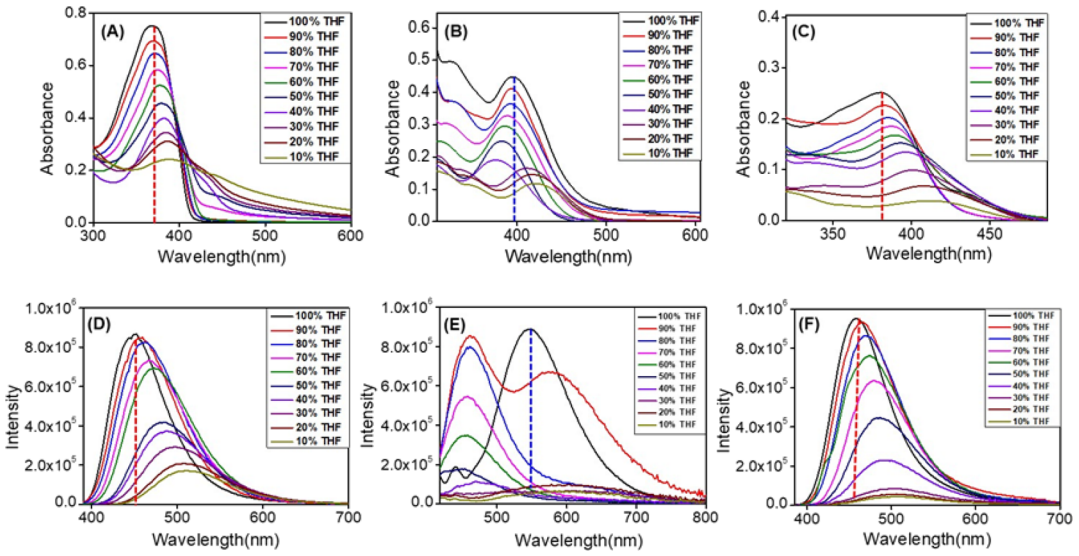

Figure 1. UV−vis absorbance spectra of **TP** (A) and **TPZn** (B) and $(\mathbf{TP})_2\mathbf{Zn}$ (C) in THF and the THF−aqueous medium. Fluorescence spectra of **TP** (D) and **TPZn** (E) and $(\mathbf{TP})_2\mathbf{Zn}$ (F) in THF and the THF−aqueous medium (λ_{Ext} = 368 nm for **TP**, λ_{Ext} = 395 nm for **TPZn**, and λ_{Ext} = 380 nm for $(\mathbf{TP})_2\mathbf{Zn}$).

tions.[12,37−39] On the other hand, terpyridine and its derivatives, especially the 4-substituted one, are well recognized in supramolecular chemistry due to their extended π-conjugation and their ability to coordinate with different transition metal ions.[40−43] The excellent photophysical, electrochemical, and catalytic properties[44−48] of these terpyridine derivatives and their corresponding metal complexes have led to finding their potential uses in numerous areas such as sensors, solar cells, energy storage, and molecular electronics.[49] Therefore, the design of a small π-conjugated molecular system having both these phenanthro[9,10-*d*]imidazole and 4-substituted terpyridine moieties is extremely desirable from a supramolecular point of view and expected to exhibit characteristic tunable self-assembly and optical and electronic properties, which can make this system a promising module for device applications.

Herein, we report the synthesis of a low-molecular-weight π-conjugated molecule (**TP**) (phenanthro[9,10-*d*]imidazole with terpyridine substitution at the 2 position) and its corresponding 1:1 and 1:2 Zn(II) complexes (**TPZn** and $(\mathbf{TP})_2\mathbf{Zn}$). We investigated the representative photophysical behavior with solvent polarity-induced tunable optical and self-assembly properties of this π-conjugated molecule (**TP**) and its corresponding metal complexes (**TPZn** and $(\mathbf{TP})_2\mathbf{Zn}$) and described the probable mechanistic aspects of the medium polarity-triggered self-assembly-based morphological transformation associated with tunable optical responses. Our experimentally investigated results were further validated by the density functional theory (DFT) studies, which clarify how the metal coordination to this π-conjugated system (**TP**) impacts the energy difference between the donor−acceptor molecular energy levels, which is responsible for multiple optical outcomes. Furthermore, the basic behavior of an electronic device can be appraised by the current and current density−voltage (I&J−V) characteristics, which reflect the relationship between the currents through an electronic device and the applied voltages in an electrical circuit and exploited to examine the material properties such as conductivity, charge carrier mobility, and charge injection efficiency.[50−53] Herein, we also investigate the I−V characteristics of **TP**, **TPZn**, and $(\mathbf{TP})_2\mathbf{Zn}$ to evaluate their possible potential utility in electronic device fabrication.

RESULTS AND DISCUSSION

We synthesized a phenanthro[9,10-*d*]imidazole and 4-substituted terpyridine-based π-conjugated molecule 2-(4-[2,2′:6′,2″]-terpyridine-4′-yl-phenyl)-1*H*-phenanthro[9,10-*d*]-imidazole (**TP**) and its corresponding monotridentate and bistridentate Zn(II) complexes, **TPZn** and $(\mathbf{TP})_2\mathbf{Zn}$, respectively. **TP** was synthesized by refluxing a mixture of 9,10-phenanthrenequinone with 4′-(*p*-formyl phenyl)-2,2′:6′,2″-terpyridine in the presence of excess ammonium acetate in glacial acetic acid medium. The metal complexes **TPZn** and $(\mathbf{TP})_2\mathbf{Zn}$ were synthesized by reacting an aqueous solution of $ZnCl_2$ with a methanolic solution of **TP** having different concentrations (Scheme 1). In **TPZn**, two chloride ions coordinated with the Zn(II) center, and in $(\mathbf{TP})_2\mathbf{Zn}$, two chloride ions presented as counteranions, which were further supported by elemental analysis. The complete synthetic procedures of 4′-(*p*-formyl phenyl)-2,2′:6′,2″-terpyridine, **TP**, **TPZn**, and $(\mathbf{TP})_2\mathbf{Zn}$ are provided in the experimental section of the Supporting Information (Schemes S1 and S2) with appropriate analytical characterization (Figures S1−S7).

It is well established that the polarity of the solvent medium has a substantial impact on the self-assembly properties of molecules having hydrogen bonding sites and hydrophobic groups.[54−56,19] Furthermore, it was also observed that the overall self-assembly direction of the π-conjugated system is controlled by the polarity of the self-assembly medium.[12,55] We investigated the influence of medium polarity on the self-assembly and optical properties of this π-conjugated molecule (**TP**) and its corresponding monotridentate and bistridentate Zn(II) complexes (**TPZn** and $(\mathbf{TP})_2\mathbf{Zn}$). Solvent polarity-induced alternation in the nature of noncovalent forces as well as the morphological transformation of the self-assembled states due to the change in the aggregation pattern was examined by spectroscopic as well as microscopic techniques. At first, we recorded the absorption spectra of **TP** in THF and an aqueous-THF mixture having different polarities.

https://doi.org/10.1021/acsomega.3c06283
ACS Omega 2023, 8, 48855−48872

The UV−vis absorption spectra of **TP** (20 μM) in a pure THF solvent medium showed an absorption band maximum at 368 nm ($\varepsilon = 3.7 \times 10^4$ M^{-1} cm^{-1}), which can be ascribed to the spin-allowed intramolecular charge transfer (ICT) band (Figure 1A). Upon a gradual increase of the medium polarity by increasing the proportion of water in THF and water mixtures, there is a steady decrease in the intensity of the characteristic ICT band (Figure 1A) as the polar solvent facilitates the self-assembly process of the molecular building blocks.[57] Ultimately, in 90% aqueous-THF medium, the absorption maxima appeared at 389 nm with a distinctive redshift of ∼49 nm with another broad shoulder peak in the visible region at 438 nm (Figure 1A). This type of redshift of the CT absorption maxima is expected for J-type aggregation. The absorption spectral behavior of **TPZn** and $(\mathbf{TP})_2\mathbf{Zn}$ in THF-aqueous mixtures with varying polarities was also studied. For **TPZn**, in 100% THF medium, the absorption maxima appeared at 395 nm ($\varepsilon = 2.2 \times 10^4$ M^{-1} cm^{-1}) (Figure 1B), and for $(\mathbf{TP})_2\mathbf{Zn}$, it appeared at 380 nm ($\varepsilon = 1.2 \times 10^4$ M^{-1} cm^{-1}) (Figure 1C). Zn(II) coordination with the terpyridine unit significantly influences the intraligand charge transfer property because coordinated terpyridine is a better electron acceptor than the free terpyridine moiety of **TP** and experienced a substantial bathochromic shift of the ICT band. **TPZn** displayed a noticeable fall in the intensity of the absorption maxima with increasing medium polarity. Furthermore, with the stepwise increment of water content in the solvent medium, the CT band exhibited a gradual hypochromic shift due to the operational molecular association process in the polar medium. This blueshift was apparent from 10% aqueous-THF medium up to 60% aqueous-THF medium. This type of blueshift of the CT band was anticipated for H-type aggregation, a renowned significance of Kasha's theory that blue-shifted absorption maxima displayed due to H-aggregation.[58,59] Further, in highly polar 70% (water−THF 7:3 (v/v)) to 90% (water−THF 9:1 (v/v)) aqueous-THF medium, the CT absorption maxima of **TPZn** experienced a noticeable redshift and appeared at 420 nm. The appearance of red-shifted absorption maxima in a highly polar medium with a higher percentage of water content is due to the alternation of the operative intermolecular noncovalent interactions, which affects the molecular order during the molecular association process and causes the lowering of HOMO−LUMO-related energy gap associated with electronically rich and poor moieties. We also recorded the UV−vis absorption spectra of $(\mathbf{TP})_2\mathbf{Zn}$ in an aqueous-THF medium with different percentages of water. In 100% THF, the CT absorption maxima appeared at 380 nm ($\varepsilon = 1.2 \times 10^4$ M^{-1} cm^{-1}). Upon further increase of the polarity of the medium with a gradual increase of water percentage, there is a considerable steady redshift of the CT absorption maxima. In a 9:1 aqueous-THF medium (water−THF 9:1 (v/v)), this CT absorption maxima appeared at 411 nm with an eventual redshift of ∼23 nm. In **TPZn** (1:1 complex), there are available coordination sites for Zn(II) (d^{10} system). Therefore, in a polar medium with a high content of water, the H_2O molecule probably binds with Zn(II) and drives the molecular association with enhanced intermolecular hydrogen bonding. Meanwhile, for $(\mathbf{TP})_2\mathbf{Zn}$, this possibility is much less due to the lesser availability of accessible coordination sites of Zn(II). In the case of **TPZn**, two chloride ligands attached with the Zn(II) center in solvent medium from 10 to 60% aqueous THF and exhibited a gradual blueshift of absorption maxima associated with H-aggregation. But upon further increment of water content, the coordinated chloride ligands are replaced by water molecules, which provide additional intermolecular H-bonding and stabilize the electronic excited state relative to the ground state, resulting in the redshift of the absorption maxima associated with J-aggregation.

To examine the stability of the self-assembled structures, we recorded the temperature-dependent UV−vis spectra of **TP**, **TPZn**, and $(\mathbf{TP})_2\mathbf{Zn}$ in 90% aqueous medium. This result showed that the self-assembled structures remained almost unchanged up to 70 °C and revealed the high thermal stability of the fabricated structures obtained from **TP**, **TPZn**, and $(\mathbf{TP})_2\mathbf{Zn}$ (Figure S8). Furthermore, thermogravimetric analysis (TGA) revealed that **TP**, **TPZn**, and $(\mathbf{TP})_2\mathbf{Zn}$ were stable up to 347, 273, and 255 °C, respectively (Figure S9).

To get a better insight into the molecular association process and to understand the effects of the aggregation on the emission properties of **TP**, **TPZn**, and $(\mathbf{TP})_2\mathbf{Zn}$, we have performed steady-state fluorescence measurements in aqueous-THF medium with different percentages of water. In 100% THF medium, the emission spectra of **TP** appeared with an emission maximum at 450 nm (λ_{Ext} = 368 nm) (Figure 1D). In 90% THF medium (water−THF 1:9 (v/v)), the emission maxima experienced an appreciable bathochromic shift and appeared at 458 nm. Upon further increase of medium polarity by increasing the water percentage, there is a steady decrease in emission intensity associated with a gradual redshift of emission maxima. In 90% aqueous-THF medium (water−THF 9:1 (v/v)), the emission maxima appeared at 512 nm with an eventual redshift of ∼62 nm. The characteristic features of the emission spectra of **TP** in different solvent media with varying polarities are in good agreement with the fact that the lowest-energy emission in a less polar medium (100% THF) is strongly dipole-allowed for J-type aggregation but prohibited for H-aggregation.[59] On the other hand, the emission spectra of **TPZn** in a THF−water mixture with varying proportions exhibited a substantial alternation in the spectral behavior as well as emission output. In 100% THF medium, the emission band of **TPZn** appeared with an emission maximum at 546 nm (λ_{Ext} = 395 nm) (Figure 1E). In a 10% aqueous-THF (water−THF 1:9 (v/v)) medium, the emission spectra displayed two distinct emission bands. One is red-shifted and appeared at 578 nm, and another one is blue-shifted and appeared at 462 nm. In 20% aqueous-THF (water−THF 2:8 (v/v)), the emission spectra displayed a single emission maximum at 459 nm. Upon further increase of medium polarity up to 50% aqueous-THF medium (water−THF 1:1 (v/v)), we observed a steady decrease of emission intensity, associated with a steady hypochromic shift. In a 1:1 aqueous-THF medium, the emission band exhibited a blue-shifted emission maximum at 448 nm. Upon a further increment of water percentage in the THF−water mixture, an appreciable redshift of the emission maxima was observed. Finally, in a 90% aqueous-THF medium (water−THF 9:1 (v/v)), a weak and broad emission band appeared with an emission maximum at 608 nm. It was previously discussed that a minimal association or aggregation between two building blocks can be described in two possible categories based on either constructive (J-type aggregation) or destructive (H-type aggregation) combination of the two molecular transition moments, resulting in the lower-energy excitonic state.[60] Within the limit of strong coupling, the electronic spectra (both UV−vis and fluorescence) are red-shifted for J-

https://doi.org/10.1021/acsomega.3c06283
ACS Omega 2023, 8, 48855−48872

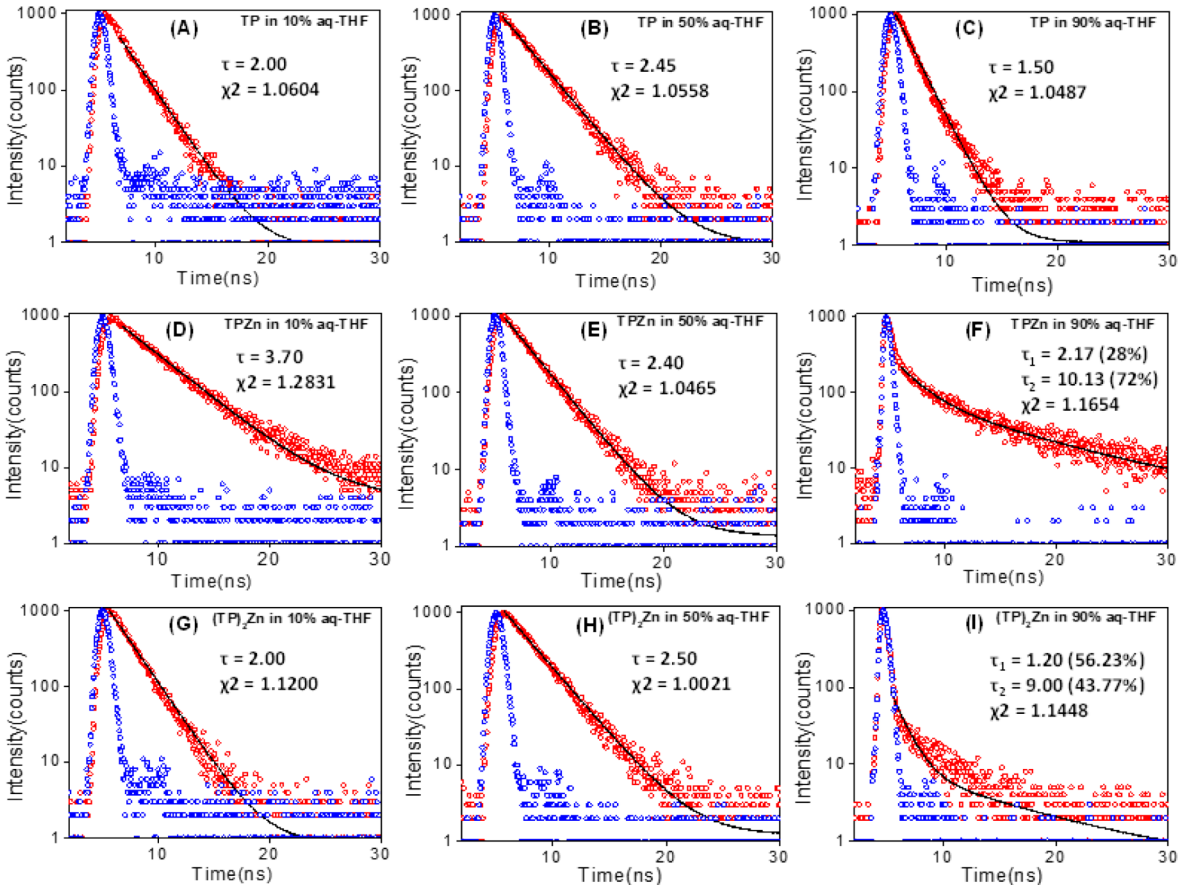

Figure 2. Time-resolved emission decay profile for (A) **TP** at λ_{Mon} = 458 nm, λ_{Ext} = 369 nm in 10% aqueous-THF; (B) **TP** at λ_{Mon} = 484 nm, λ_{Ext} = 379 nm in 50% aqueous-THF; (C) **TP** at λ_{Mon} = 512 nm, λ_{Ext} = 389 nm in 90% aqueous-THF; (D) **TPZn** at λ_{Mon} = 462 nm, λ_{Ext} = 395 nm in 10% aqueous-THF; (E) **TPZn** at λ_{Mon} = 448 nm, λ_{Ext} = 382 nm in 50% aqueous-THF; (F) **TPZn** at λ_{Mon} = 608 nm, λ_{Ext} = 420 nm in 90% aqueous-THF; (G) $(\mathbf{TP})_2\mathbf{Zn}$ at λ_{Mon} = 463 nm, λ_{Ext} = 381 nm in 10% aqueous-THF; (H) $(\mathbf{TP})_2\mathbf{Zn}$ at λ_{Mon} = 485 nm, λ_{Ext} = 393 nm in 50% aqueous-THF; and (I) $(\mathbf{TP})_2\mathbf{Zn}$ at λ_{Mon} = 507 nm, λ_{Ext} = 411 nm in 90% aqueous-THF. The 450 and 380 nm LEDs are used as excitation sources.

aggregation and blue-shifted with comparatively weak emission for H-aggregation. The spectral consequences of **TPZn** with varying medium polarities revealed the molecular association through H-aggregation. Furthermore, in a highly polar medium, the red-shifted broad emission band in the visible region can be predicted for strongly coupled J-aggregation.[60] In principle, both the bathochromic shift and hypochromic shift could originate from a single-type aggregation (same ground state) or different types of aggregation due to diverse packing structures of the monomeric building block.[60]

Further, we have also recorded the emission spectra of $(\mathbf{TP})_2\mathbf{Zn}$ in aqueous-THF medium with varying water proportions. In 100% THF, $(\mathbf{TP})_2\mathbf{Zn}$ displayed an emission band with an emission maximum of 458 nm (Figure 1F). Upon a gradual increase of medium polarity, there is a steady fall in emission intensity with a substantial bathochromic shift of the emission maxima. In a highly polar 9:1 aqueous-THF medium, a broad emission band appeared having an emission maximum at 507 nm with an eventual redshift of ∼50 nm. The solvent polarity-induced spectral patterns suggested that the lowest-energy emission was promptly dipole-allowed for J-aggregation but forbidden for H-type aggregation. The spectral consequences of $(\mathbf{TP})_2\mathbf{Zn}$ with varying medium polarities revealed the J-type aggregation during molecular association.

Sometimes, the limited photoluminescence (in vivo) of currently available optical probes restricts their adaptability and applicability for determining the imaging contrast effect. This is mainly due to the uncontrollable aggregation of the monomeric optical probes that causes emission quenching. On the other hand, optical probes having extended π-conjugation composed of donor and/or acceptor couples are susceptible to exhibiting aggregation-caused quenching (ACQ). Recently, Yan et al. described the design and synthesis of self-assembling NIR cyanine-based nanoprobes with an enhanced TPA (two-photon absorption) fluorescence imaging property displaying a photo-oxidation-enhanced emission mechanism.[61] In this context, **TP**, **TPZn**, and $(\mathbf{TP})_2\mathbf{Zn}$ with π-conjugated planar structures are able to display polarity-induced aggregation with strong as well as tunable emission properties. This polarity-induced controllable aggregation can able to restrict the intramolecular motion and avoid the ACQ effect responsible for strong emission in aggregated states.

This conclusion is further supported by the fluorescence lifetime measurement by time-correlated single photon counting. The fluorescence lifetime measurement was carried out for **TP**, **TPZn**, and $(\mathbf{TP})_2\mathbf{Zn}$ in 10% aqueous-THF, 50% aqueous-THF, and 90% aqueous-THF medium at their respective emission maxima using 380 and 450 nm lasers as the excitation sources (Figure 2). The decay profile of **TP** in 10% aqueous-THF medium (λ_{Mon} = 458 nm) exhibited a single time constant, τ_1 = 2.0 ns (Figure 2A). Upon increasing the polarity up to 50% aqueous-THF medium, the decay

https://doi.org/10.1021/acsomega.3c06283
ACS Omega 2023, 8, 48855−48872

profile at its respective emission maxima (λ_{Mon} = 484 nm) revealed a single-component decay profile with a time constant value (τ_1) of 2.45 ns (Figure 2B). In 90% aqueous-THF medium at respective emission maxima (λ_{Mon} = 512 nm), the TCSPC studied displayed a single-component-based decay profile with a lower time constant value (τ_1) of 1.50 ns (Figure 2C). Similarly, for **(TP)$_2$Zn**, at a 10% aqueous-THF medium (λ_{Mon} = 463 nm), it showed a single-component-based fluorescence decay profile (τ_1 = 2.05 ns) (Figure 2G), and in a more polar 50% aqueous-THF medium, the time constant value was slightly increased (τ_1 = 2.5 ns) (Figure 2H). These values of time constants are very similar to the lifetime components of **TP** in similar solvent systems at their corresponding emission maxima. Moreover, upon further increase of medium polarity, in a 9:1 aqueous-THF medium, the biexponential decay profile of **(TP)$_2$Zn** revealed two different time constants (τ_1 = 1.25 ns (56.23%), τ_2 = 9.0 ns (43.77%), χ^2 = 1.14) with the longer component as the minor one and the shorter component as the major one (Figure 2I). These characteristics of the decay profile revealed that in highly polar solvents, the lowest-energy strongly dipole emission maxima preferred the J-type aggregation. On the other hand, in a less polar 10% aqueous-THF medium, the decay profile for **TPZn** (λ_{Mon} = 462 nm) displayed a single time constant, τ_1 = 3.70 ns, χ^2 = 1.28 (Figure 2D). In a 1:1 aqueous-THF medium, the fluorescence decay traces recorded for **TPZn** at respective emission maxima (λ_{Mon} = 448 nm) showed a single decay constant (τ_2 = 2.4 ns, χ^2 = 1.04), which is less than the time constant value at the respective monitoring wavelength in a less polar 10% aqueous-THF medium (Figure 2E). In a highly polar medium with 90% water (water−THF 9:1 (v/v)), the recorded fluorescence decay traces revealed a biexponential decay profile for **TPZn** (τ_1 = 2.17 (28%), τ_2 = 10.13 ns (72%), χ^2 = 1.14) (Figure 2F). The longer and major component for **TPZn** can be ascribed to the ICT state. It is well-known that in the polar medium, the unusual vibronic patterns exhibited during the aggregation are intermediate between those of the monomeric units and aggregated form. In a highly polar medium, with the highest percentage of water (90% aqueous-THF), for **TPZn**, the longer component of the decay constants is the major one, while for **(TP)$_2$Zn**, the shorter component of the time constants is the major one. This result suggests that in a less polar medium with less percentage of water the inconsistent vibronic structure of the aggregates is mainly due to the coexistence of monomeric and aggregated states. With increasing the percentage of water, both **TPZn** and **(TP)$_2$Zn** aggerate differently, and this discrepancy is also reflected in their solvent polarity-induced electronic spectral pattern as well as in the respective relative percentage of their decay components. Furthermore, the proposed J-type aggregation for **TP** and **(TP)$_2$Zn** and H-type aggregation for **TPZn** were further supported by the photoluminescence quantum yield measurement. We measured the quantum yields for **TP**, **TPZn**, and **(TP)$_2$Zn** in THF and 50% aqueous-THF medium. Upon the medium polarity, there is a noticeable increase in the emission quantum yield for **TP** and **(TP)$_2$Zn** from 28 to 42 and 22 to 39% respectively, which supports the J-type aggregation.[62] On the other hand, a substantial decrease in the emission quantum yield for **TPZn** from 20 to 3% upon increasing the medium polarity supports the H-type aggregation due to the self-quenching and excitonic interactions between the **TPZn** monomers in close proximity.[63]

We also carefully investigated the visually detectable emission colors generated by **TP**, **TPZn**, and **(TP)$_2$Zn** in different THF−water mixed solvent media with varying proportions of water. It was observed that for **TP**, there was a noticeable change in the brightness of the characteristic blue fluorescence with increasing solvent polarity (Figure 3A).

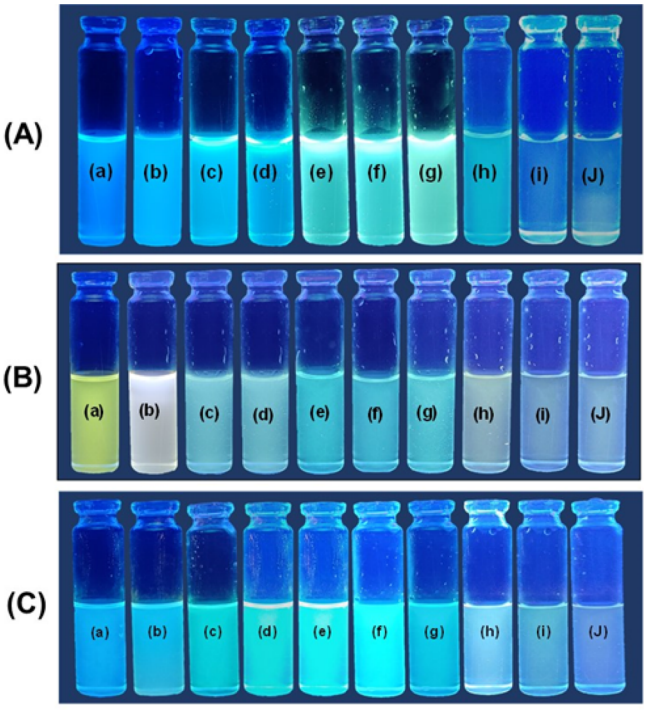

Figure 3. Photographs showing the change in the fluorescence colors of (A) **TP**, (B) **TPZn**, and (C) **(TP)$_2$Zn** upon irradiation with 365 nm light at different ratios of the THF/H_2O mixture.

Initially, in up to 30% aqueous-THF medium, **TP** displayed a characteristic blue fluorescence. Upon further increase of water percentage, it exhibited green fluoresce, and in a highly polar medium (90% aqueous-THF medium), the fluorescence gets quenched due to aggregation-induced quenching (AIQ).[64,65] A similar type of emission color output was also observed for **(TP)$_2$Zn** (Figure 3C). Most interestingly, in both cases, we observed a considerable redshift of absorption as well as emission maxima with increasing medium polarity due to anticipated J-type aggregation. Meanwhile, for **TPZn**, there is a significant change in the emission color from yellow to white to green with varying the water percentage from 0 to 50% (Figure 3B). With increasing medium polarity from 100% THF to 50% aqueous-THF, **TPZn** exhibited a steady blueshift of the characteristic absorption and emission maxima due to predicted H-type aggregation. For **TPZn**, in 10% aqueous-THF medium, the fluorescence spectra covered the complete visible region (~400 to 700 nm) and were responsible for white light emission. In a highly polar medium with a higher percentage of water (90% aqueous-THF medium), the intensity of the emission color was significantly reduced due to the AIQ (Figure 3B).

The perceptible changes in the optical property in different THF−water mixtures with varying polarities are due to the change in the aggregation pattern of these monomeric building

https://doi.org/10.1021/acsomega.3c06283
ACS Omega 2023, 8, 48855−48872

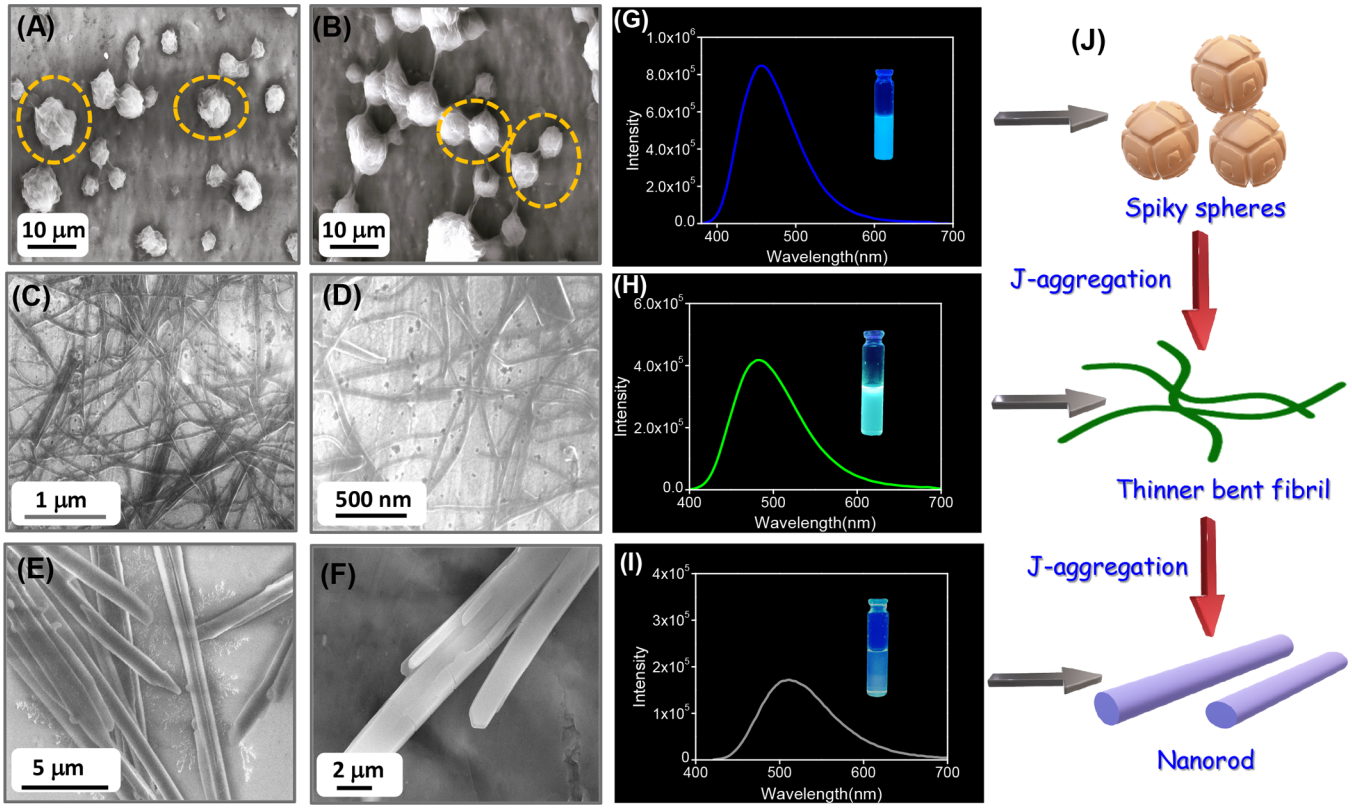

Figure 4. HR-SEM micrographs of the self-assembled structures formed by **TP** in 10% aqueous-THF (A, B), 50% aqueous-THF (C, D), and 90% aqueous-THF (E, F). Emission spectra and luminescence colors of self-assembled **TP** were obtained in 10% aqueous-THF (G), 50% aqueous-THF (H), and 90% aqueous-THF (I). (J) Pictorial representation of the various self-assembled structures with different morphologies formed by building block **TP** in THF−water mixed solvents of varying polarities; formation of various superstructures formed due to different organizations of the monomeric building blocks.

blocks with induced medium polarity. Therefore, morphological individualities of the self-assembled structures can be expected from **TP**, **TPZn**, and $(\mathbf{TP})_2\mathbf{Zn}$ in different THF−water media with varying polarities owing to the alternation in the composite combination of various noncovalent forces. In this regard, we have explored the self-assembly property of **TP**, **TPZn**, and $(\mathbf{TP})_2\mathbf{Zn}$ in THF−water mixtures with varying percentages of water. In 10% aqueous-THF medium, **TP** self-assembled into spiky spherical aggregates (Figure 4A,B). With a higher proportion of water, in 50% aqueous-THF medium, **TP** is fabricated into bent and thinner fibrils and forms a fibrillar network (Figure 4C,D). Upon further increase of the polarity of the self-assembly medium, in 90% aqueous-THF medium, **TP** self-assembles into nanorods (Figure 4E,F). The emission spectra of **TP** in 10, 50, and 90% aqueous-THF medium showed a significant bathochromic shift of the emission maxima with increasing polarity of the self-assembly medium with a substantial change in the emission color (Figure 4G−I). Figure 4J shows the morphological transformation of the self-assembled structures formed by **TP** with increasing polarity of the self-assembly medium.

On the other hand, **TPZn** is self-assembled into various supramolecular structures with different morphologies in an aqueous-THF medium with varying percentages of water. In 10% aqueous-THF medium, **TPZn** self-assembled into elongated nanofibers (Figure 5A,B), which upon further increment of water percentage (50% aqueous-THF medium) fabricated into a nanobelt-like morphology (Figure 5C,D). In a highly polar 90% aqueous-THF medium, **TPZn** self-assembles into broken nanorod-like structures (Figure 5E,F). Similarly, the self-assembled **TPZn** in 10, 50, and 90% aqueous-THF medium generated multiple luminescence colors (Figure 5G−I). Figure 5G represents the fabrication of different self-assembled structures with various morphologies by **TPZn** in different self-assembly media of varying polarities.

We also explored the self-assembly property of $(\mathbf{TP})_2\mathbf{Zn}$ in different aqueous-THF media with varying polarities. In a less polar 10% aqueous-THF medium, $(\mathbf{TP})_2\mathbf{Zn}$ fabricated into a spiky spherical assembly (Figure 6A,B), which upon increase of water percentage (1:1 aqueous-THF medium) generated a fibrillar network consisting of thicker fibrils (Figure 6C,D). Upon further increase of medium polarity (90% aqueous-THF medium), $(\mathbf{TP})_2\mathbf{Zn}$ self-assembled into a distorted nanorod-like morphology (Figure 6E,F). Fabricated $(\mathbf{TP})_2\mathbf{Zn}$ displayed different emission outputs upon varying the polarity of the self-assembly medium (Figure 6G−I). Figure 6J represents the fabrication of $(\mathbf{TP})_2\mathbf{Zn}$ into different superstructures upon varying the polarity of the self-assembly medium. This morphological variation originated from the different aggregation patterns in solvent medium with varying polarities due to the alternation in the operative noncovalent interactions.

This microscopy study (HR-SEM analysis) helps us to predict the mechanism behind the self-assembly process of **TP**, **TPZn**, and $(\mathbf{TP})_2\mathbf{Zn}$ in different solvent systems having varying polarities. It was proposed that the monomeric unit of **TP** be fabricated into a spiky spherical assembly mainly through aromatic π-stacking and an intermolecular H-bonding interaction. Upon increasing the polarity of the self-assembly

https://doi.org/10.1021/acsomega.3c06283
ACS Omega 2023, 8, 48855−48872

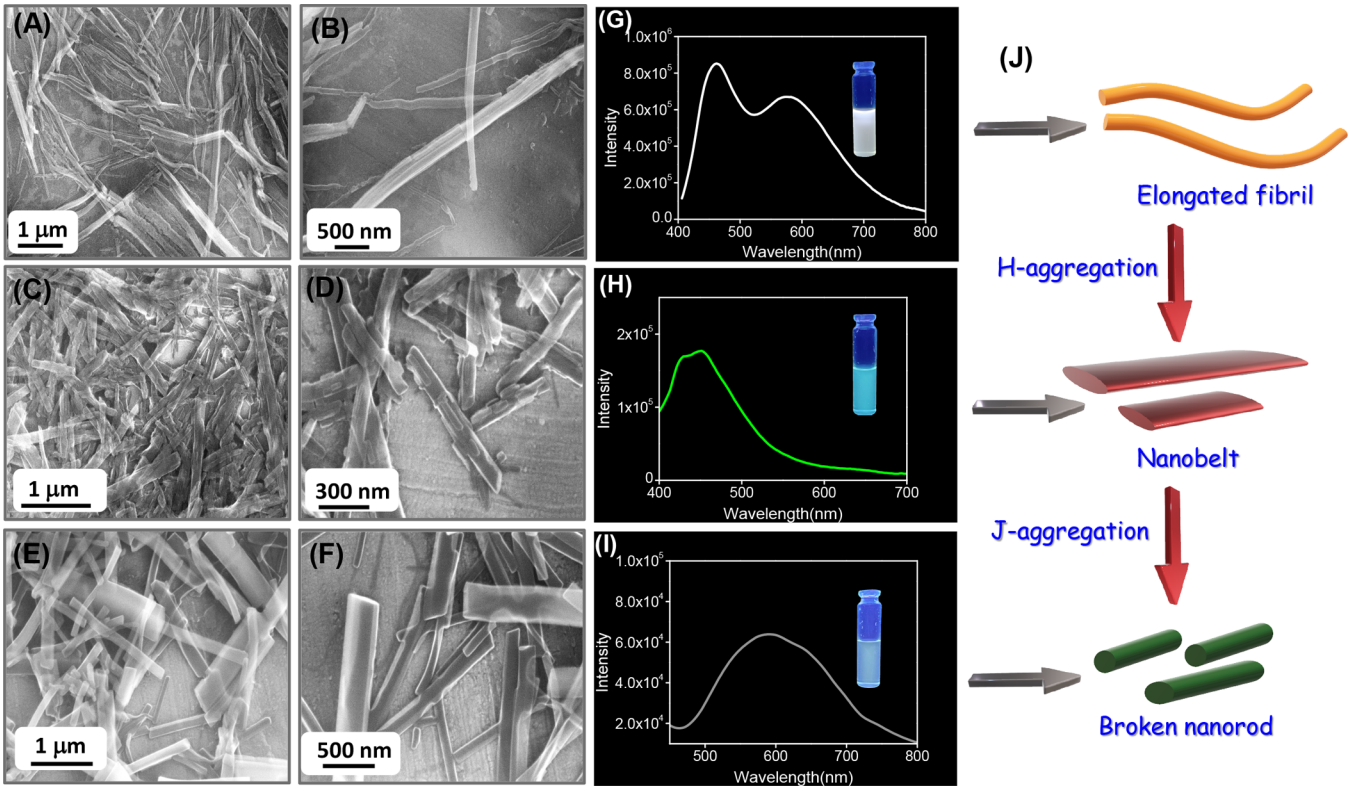

Figure 5. HR-SEM micrographs of the self-assembled structures formed by **TPZn** in 10% aqueous-THF (A, B), in 50% aqueous-THF (C, D), and in 90% aqueous-THF (E, F). Emission spectra and luminescence colors of self-assembled **TPZn** were in 10% aqueous-THF (G), 50% aqueous-THF (H), and 90% aqueous-THF (I). (J) Pictorial representation of the various self-assembled structures with different morphologies formed by building block **TPZn** in THF−water mixed solvents of varying polarities; formation of various superstructures formed due to different organizations of the monomeric building blocks.

medium, the presence of π-conjugated systems promoted the molecular aggregation process due to the greater hydrophobic forces. The increment of water percentage in the self-assembly medium promotes the self-aggregation process to minimize the water-induced hydrophobic interactions as well as surface energy of the fabricated assembly, which triggers the morphological transformation from a spiky sphere to a thin fibril to a nanorod with increasing medium polarity.[66] Proper tuning of degree of desolvation at different stages of self-assembly can effectively control the self-assembly pathways and polymorphisms. Recently, Yan and his co-workers showed that multistep desolvation should be considered an effective parameter to trigger the LLPS (liquid−liquid phase separation)-mediated self-assembly of the peptide-based monomer, which is different from the classical one-step peptide-based self-assembly.[67] This clearly displayed the role of the solvent in controlling the overall self-assembly process. In another work, they described the formation of amorphous biomolecular glasses with appreciable biodegradability, biorecyclability, and excellent optical characteristics from chemically modified amino acids and peptides using a classic heating-quenching procedure. This result clearly revealed that the absolute change in thermodynamic and kinetic parameters effectively controlled the self-assembly process with morphological transition.[68] Scheme 2 shows the stepwise fabrication of **TP**, **TPZn**, and $(\mathbf{TP})_2\mathbf{Zn}$ into different self-assembled structures with morphological individualities in 90% aqueous-THF medium of varying polarities.[19,54,69]

The modes of the molecular aggregation of **TP**, **TPZn**, and $(\mathbf{TP})_2\mathbf{Zn}$ in a highly polar 90% aqueous-THF medium were further confirmed from PXRD analysis of the dried mass of these compounds obtained from a 9:1 aqueous-THF medium. The diffraction peaks at 23.4, 24.5, 25.4, and 26.8° (with respective *d*-spacing values of 3.8, 3.5, 3.4, and 3.3 Å) for **TP** (Figure 7A); 20.5, 21.6, and 26.9° (with respective *d*-spacing values of 4.3, 4.1, and 3.3 Å) for **TPZn** (Figure 7B); and 23.3 and 26.0° (with respective *d*-spacing values of 3.8 and 3.4 Å) for $(\mathbf{TP})_2\mathbf{Zn}$ (Figure 7C) suggest the existence of an operational $\pi-\pi$ stacking interaction and intermolecular H-bonding among the monomeric units in the self-assembly state.

More importantly, as shown in Figure 7A, the diffraction peaks obtained for the nanorod assembly fabricated from **TP** at 8.1° followed by other peaks in the wide-angle region in a periodical order at 16.4, 24.5, and 29.9° with corresponding *d*-spacing values of 10.2, 5.3, 3.6, and 2.9 Å, respectively. The periodic ratios of 1/2, 1/3, and 1/4 are consistent with the lamellar arrangement of **TP** during self-assembly, indicating the fabrication of nanorods through the layered array of **TP**. Therefore, the polarity-induced morphological transformation of **TP** can be elucidated by the following probable mechanism (Scheme 2). In a THF medium, in the absence of hydrophobic interactions, **TP** self-assembles into a spiky sphere-like assembly. Upon a gradual increase of water content in the self-assembly medium, the hydrophobic aromatic rings and highly polar imine bond of **TP** were exposed to the water molecule and attained a highly ordered multilayer molecular arrangement, which is stabilized by operational hydrophobic $\pi-\pi$ interactions and intermolecular hydrogen bonding. This precise combination of these noncovalent forces generated thinner fibrils in 50% aqueous-THF medium followed by

https://doi.org/10.1021/acsomega.3c06283
ACS Omega 2023, 8, 48855−48872

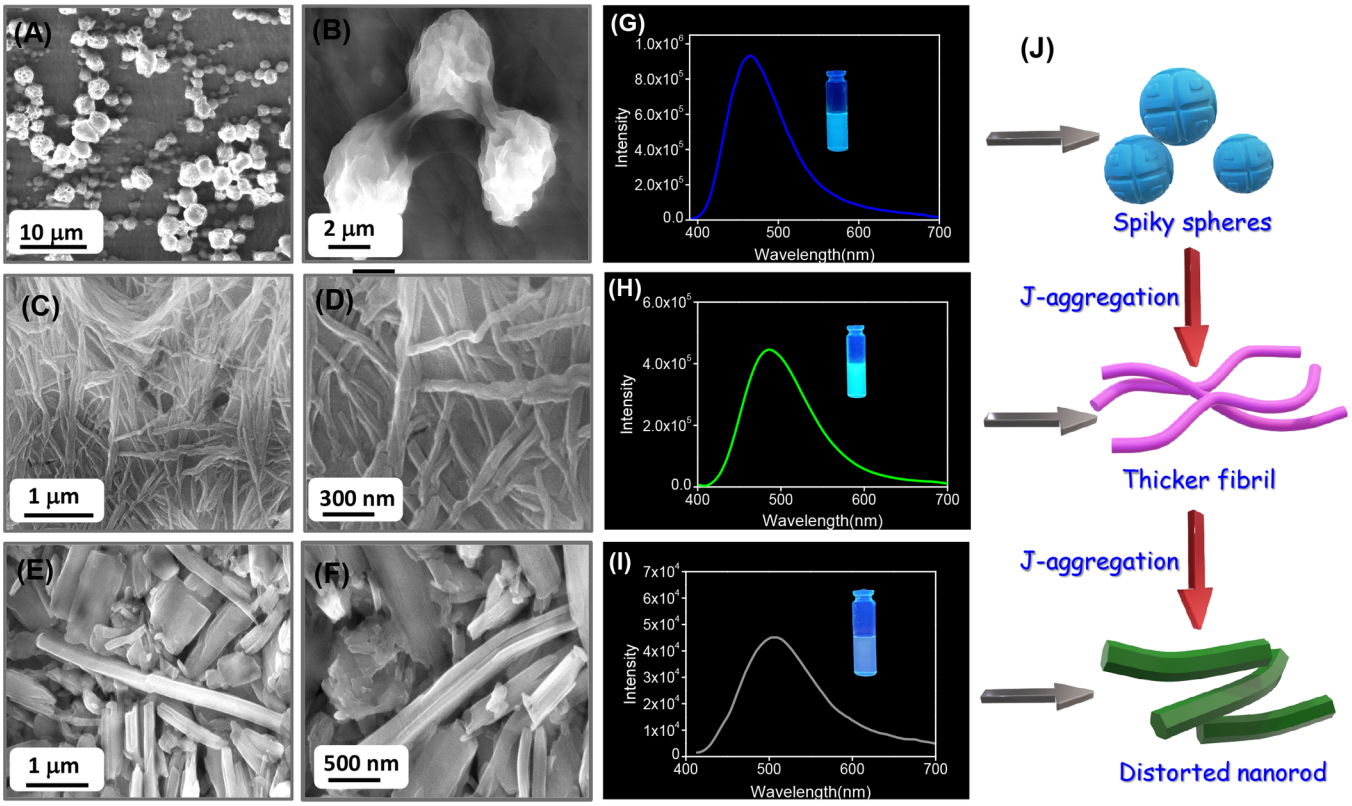

Figure 6. HR-SEM micrographs of the self-assembled structures formed by $(TP)_2Zn$ in 10% aqueous-THF (A, B), 50% aqueous-THF (C, D), and 90% aqueous-THF (E, F). Emission spectra and luminescence colors of self-assembled $(TP)_2Zn$ in 10% aqueous-THF (G), 50% aqueous-THF (H), and 90% aqueous-THF (I). (J) Pictorial representation of the various self-assembled structures with different morphologies formed by building block $(TP)_2Zn$ in THF−water mixed solvents of varying polarities; formation of various superstructures formed due to different organizations of the monomeric building blocks.

Scheme 2. Schematic Illustration of the Formation of Different Self-Assembled Structures by the Self-Assembly of TP, TPZn, and $(TP)_2Zn$ in 90% Aqueous-THF Medium through an Intermediate Lamellar Molecular Arrangement, Followed by a Layer Closure or Scroll-up Process

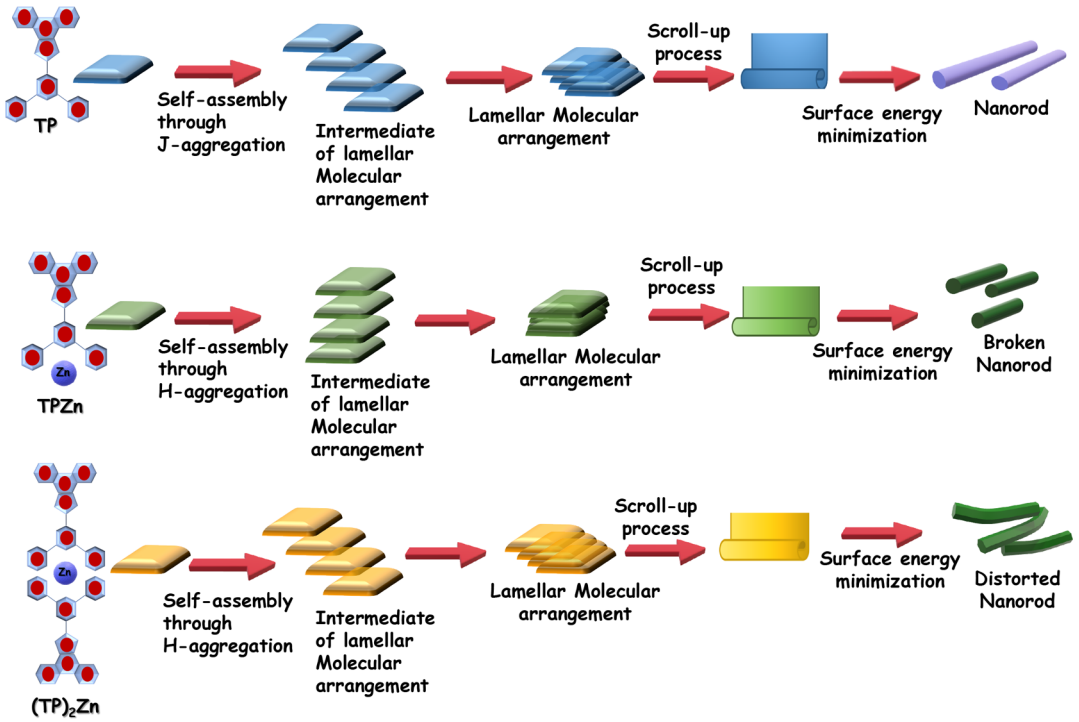

https://doi.org/10.1021/acsomega.3c06283
ACS Omega 2023, 8, 48855−48872

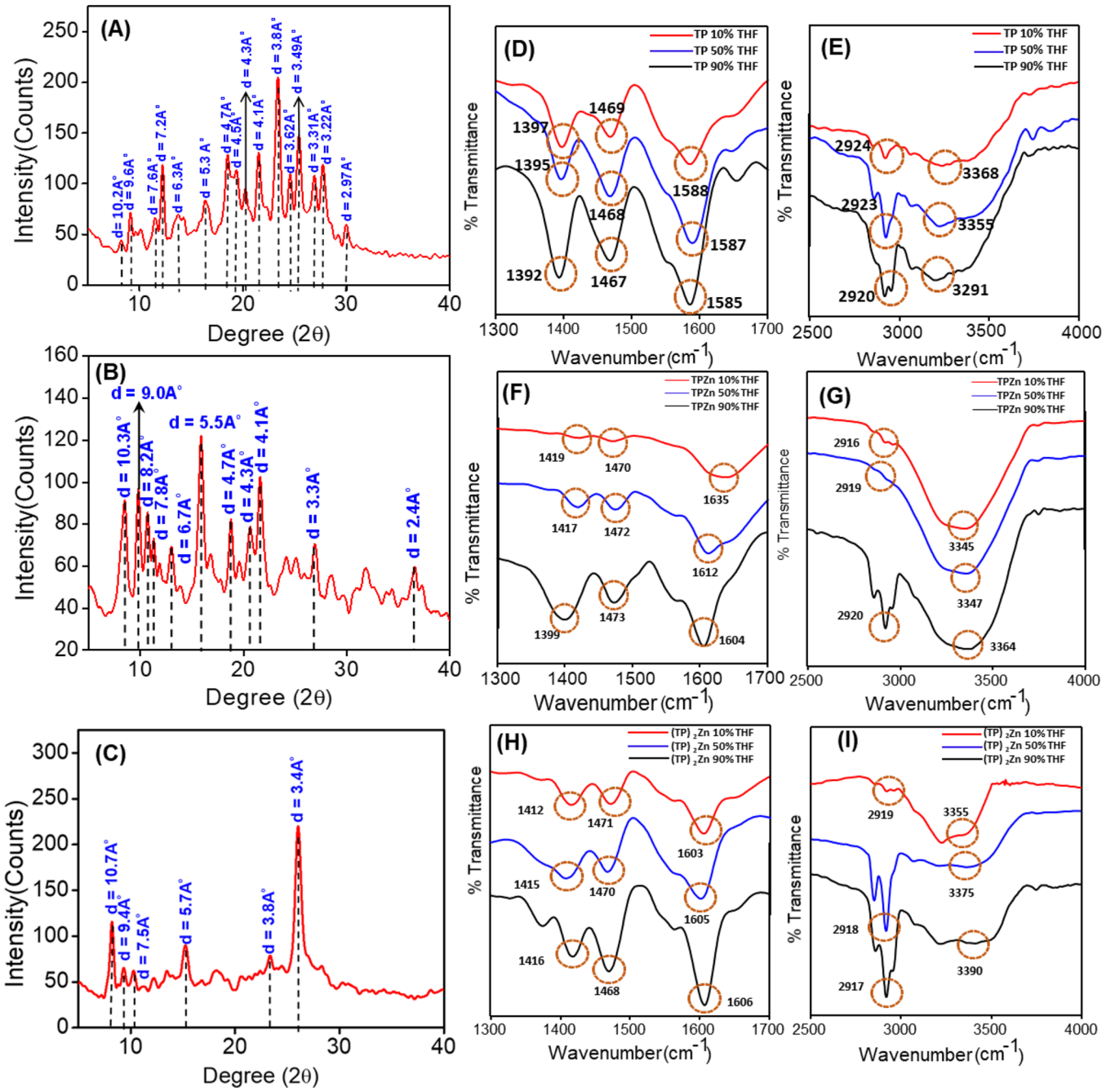

Figure 7. PXRD patterns of the dried masses of (A) **TP**, (B) **TPZn**, and (C) **$(TP)_2Zn$** obtained from 90% aqueous-THF medium. FT-IR spectra of the dried mass of (D, E) **TP**, (F, G) **TPZn,** and (H, I) **$(TP)_2Zn$** obtained from a THF/water mixed solvent having a 10% water content (black), a THF/water mixed solvent having a 50% water content (blue), and a THF/water mixed solvent having a 90% water content (red).

entangling with each other to produce a fibrillar network. In a highly polar 90% aqueous-THF medium, this lamellar arrangement becomes energetically unstable as well as unfavorable. To achieve an energetically favorable and stable arrangement, this lamellar molecular arrangement underwent a scroll-up process and fabricated nanorods. On the other hand, for **TPZn** with metal−ligand interactions, it also exhibited different diffraction peaks in a periodical order. The PXRD pattern of the dried mass of **TPZn** obtained from 90% aqueous-THF medium exhibited several intense peaks at 9.8, 18.7, and 26.9° with the corresponding *d*-spacing values of 9.0, 4.7, and 3.3 Å, respectively, and the respective periodic ratios of 1/2, 1/3, and 1/4 are in good agreement with the predicted lamellar association. It can be presumed that in a highly polar medium with a higher percentage of water, **TPZn** can coordinate with water molecules through the Zn(II) (d^{10}) center and makes the aggregated lamellar arrangement energetically unstable and unfavorable. The scroll-up process will protect the metal-coordinated π-conjugated system from hydrophobic interactions and minimize the surface energy of the fabricated assembly. Possibly, this energy minimization process broke the nanorods obtained through the scroll-up process into small pieces and became shorter in length in a highly polar 90% aqueous-THF medium. The PXRD analysis of the dried mass obtained from the self-assembled **$(TP)_2Zn$** in 90% aqueous-THF medium exhibited diffraction peaks at 8.2,

https://doi.org/10.1021/acsomega.3c06283
ACS Omega 2023, 8, 48855−48872

9.3, 10.3, 15.3, 23.3, and 26.0° with the corresponding *d*-spacing values of 10.6, 9.4, 7.5, 5.7, 3.8, and 3.4 Å, respectively, without any periodical order. The peaks at wide-angle regions at 23.4 and 26.0° indicate the existence of $\pi-\pi$ stacking and intermolecular H-bonding interactions during molecular aggregation. Therefore, it can be presumed that for **(TP)$_2$Zn**, to get an energetically stable molecular assembly, the initially formed energetically unstable lamellar arrangement endured an inappropriate scroll-up process and generated distorted nanorods like superstructures. This improper scroll-up process minimizes the surface energy of the fabricated superstructures by providing apposite protection of the aromatic ring from the hydrophobic interaction in a highly polar medium with a higher percentage of water.[54,70−72]

The above experimental results suggested that the medium polarity-induced morphological transformation of **TP**, **TPZn**, and **(TP)$_2$Zn** was achieved through an initially formed lamellar molecular arrangement. Such a lamellar arrangement is stabilized by hydrophobic interactions and $\pi-\pi$ stacking interactions of the π-conjugated system along with the intermolecular H-bonding. Upon increasing medium polarity (with a higher percentage of water), these lamellar arrangements undergo the scroll-up process to minimize the surface energy of the fabricated assembly and decide the final morphology of the energetically favorable superstructures.

Upon varying the medium polarity, the imidazole and terpyridine moiety of **TP**, **TPZn**, and **(TP)$_2$Zn** achieved a preferable conformation to attain a delicate balance of all the probable noncovalent interactions during the self-assembly process and this elusive balance between the molecular flexibility and geometrically restricted orientation of the building blocks tuning the direction of the overall self-assembly process. Still, it is really hard to expose the actual mode of assembly without an X-ray structure. Inopportunely, we failed to provide this due to some solubility problems in the specific solvent systems.

Hereafter, we are interested to investigate the alternation in intermolecular noncovalent interactions associated with different molecular aggregation patterns of **TP**, **TPZn**, and **(TP)$_2$Zn** in different solvent media with varying polarities. In this regard, we recorded the Fourier transform infrared spectroscopy (FT-IR) spectra for the dried solid mass of **TP**, **TPZn**, and **(TP)$_2$Zn** obtained from 10% aqueous-THF, 50% aqueous-THF, and 90% aqueous-THF medium. The FT-IR spectra of **TP** (solid mass) isolated from 10% aqueous-THF medium exhibited several characteristic peaks at 1392 cm^{-1} ($\nu_{C-N,aromatic}$), 1467 cm^{-1} ($\nu_{C=C,aromatic}$), 1585 cm^{-1} ($\nu_{C=N,aromatic}$), 2920 cm^{-1} ($\nu_{C-H,aromatic}$), and 3291 cm^{-1} ($\nu_{N-H,imidazole}$). We have also recorded the FT-IR spectra of the dried mass of **TP** obtained from 50 and 90% aqueous-THF medium, respectively. We observed a noticeable change in the peak intensity of the characteristic peaks corresponding to $\upsilon_{C-N(aromatic)}$, $\upsilon_{C=N(aromatic)}$, and $\upsilon_{C=C(aromatic)}$ and peak intensity as well as peak position of the characteristic peak corresponding to $\upsilon_{NH,imidazole}$ with increasing polarity of the self-assembly medium (Figure 7D,E). Similar changes in the FT-IR spectral pattern were also observed for both **TPZn** and **(TP)$_2$Zn** (Figure 7F−I). These significant changes in peak intensity for the characteristic peaks corresponding to $\upsilon_{C-N(aromatic)}$, $\upsilon_{C=N(aromatic)}$, and $\upsilon_{C=C(aromatic)}$ evidently confirmed the alternation of the $\pi-\pi$ stacking interaction during the self-aggregation of these functional π-conjugated molecules with increasing polarity of the self-assembly medium. On the other hand, the momentous change in the peak intensity as well as peak position of the $\nu_{N-H,imidazole}$-based characteristic peak indicates the more involvement of the N−H imidazole moiety through intermolecular H-bonding during self-assembly with increasing medium polarity.[73,74]

DFT calculations were carried out to understand the geometric and electronic properties of **TP**, **TPZn**, and **(TP)$_2$Zn**. The optimized geometries are shown in Figure 8.

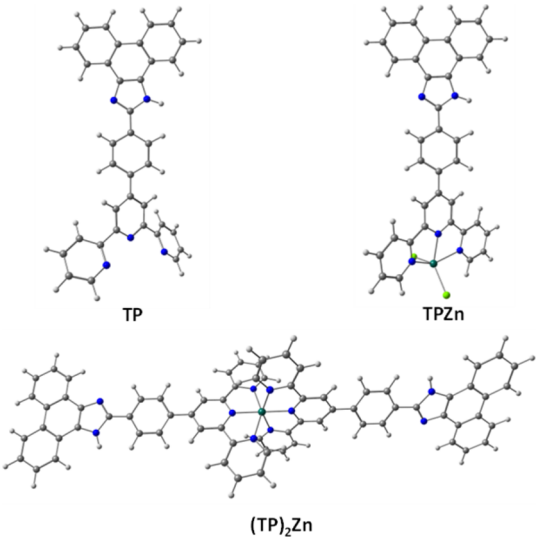

Figure 8. Geometries of **TP**, **TPZn**, and **(TP)$_2$Zn** in the gas phase optimized at the B3LYP/genECP (6-31g* for C, H, N, and Cl; SDD for Zn) level of theory using Gaussian 16 (gray, carbon; white, hydrogen; blue, nitrogen; light green, chlorine; dark green, zinc).

In **TP** and **TPZn**, the terpyridine unit is out of plane from the remainder of the molecule at a dihedral angle of 143.0° with the benzene linker. In **TPZn**, the Cl−Zn−Cl angle was observed to be 126.7°, while the Zn−Cl bond lengths were averaged to be 2.253 Å. The Zn is coordinated to the three nitrogen atoms of the terpyridine unit at an average Zn−N bond length of 2.251 Å. In the **(TP)$_2$Zn** complex, the 2 **TP** units coordinate to the Zn at perpendicular planes through the three nitrogen atoms of the terpyridines with an average Zn−N bond length of 2.19 Å. The six Zn−N coordinations in the **(TP)$_2$Zn** complex are shorter compared to those observed in **TPZn**, owing to the presence of Cl atoms that would contribute to steric repulsion in the terpyridine cavity. The frontier molecular orbitals of **TP**, **TPZn**, and **(TP)$_2$Zn** are shown in Figure 9. The contour plots of the HOMO and LUMO of **TP**, **TPZn**, and **(TP)$_2$Zn** in 100% THF solvent show that the charge density shifts indistinctly from the phenanthrene end to the terpyridine end (toward the Zn, in the case of **TPZn** and **(TP)$_2$Zn**). **TP** exhibits the highest energy gap (ΔE) of 3.621 eV, while **TPZn** has a slightly lower ΔE of 3.061 eV; this is due to the charge separation observed in their respective HOMO and LUMO. In the **(TP)$_2$Zn** complex, the ΔE is the least at 2.663 eV and a clear charge transfer state is observed as the electron density is localized on the Zn metal and the terpyridine units in the LUMO. It is evident that the charge of +2 on the **(TP)$_2$Zn** complex contributes to its lower HOMO−LUMO gap than those observed in the neutral **TP** and **TPZn**. This charge effect might influence the trend in the properties observed in the ligand and its Zn(II) complexes. Table S1 shows the HOMO, LUMO,

https://doi.org/10.1021/acsomega.3c06283
ACS Omega 2023, 8, 48855−48872

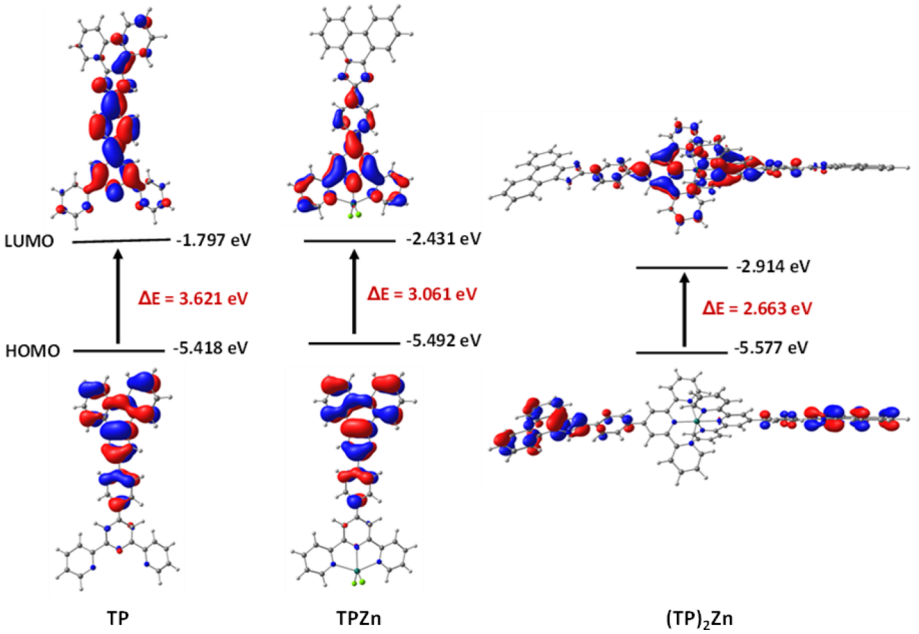

Figure 9. Molecular orbitals and their energy gaps in **TP**, **TPZn**, and $(\mathbf{TP})_2\mathbf{Zn}$ computed in 100% THF solvent (isosurface value: 0.025).

and HOMO−LUMO gap values calculated in different ratios of THF (i.e., 100% THF, 40% THF-aqueous, and 30% THF-aqueous). In **TP** and $(\mathbf{TP})_2\mathbf{Zn}$, the ΔE value decreases with a decrease in the concentration of THF solvent in the THF-aqueous solvent mixture, with the stabilization of LUMO indicating a bathochromic shift. In **TPZn**, a minor increase (of 0.005 eV) in ΔE shows that from the 100% THF to 40% THF-aqueous concentration, there is a hypsochromic shift, while in 30% THF-aqueous, it shows a slight decrease (of 0.001 eV) in ΔE values, suggesting a bathochromic shift in lower concentrations of THF solvent in the THF-aqueous solvent mixture. The observed ΔE values correspond to the spectral shifts reported in Figure 1A−C. Other electronic properties are listed in Table 1. $(\mathbf{TP})_2\mathbf{Zn}$ has the highest IE, EA, and χ of 5.577, 2.914, and 4.246 eV due to its positive charge on the Zn atom. The μ of $(\mathbf{TP})_2\mathbf{Zn}$ is least given the symmetric nature of the complex, while **TPZn** has the maximum μ owing to its high polarity, caused by the charge separation between **TP** and Cl coordination of Zn. The $(\mathbf{TP})_2\mathbf{Zn}$ complex has the least η given the low stability of the complex owing to its +2 charge, while in the solution, the charge is balanced by counter-chloride ions.

Table 1. Computed Orbital Energies (eV), Ionization Energies (IE, in eV), Electron Affinities (EA, in eV), Dipole Moments (μ, in debye), Electronegativity (χ, in eV), and Global Hardness (η, in eV) of TP, TPZn, and $(\mathbf{TP})_2\mathbf{Zn}$

parameters	TP	TPZn	$(\mathbf{TP})_2\mathbf{Zn}$
HOMO	−5.418	−5.492	−5.577
LUMO	−1.797	−2.431	−2.914
ΔE	3.621	3.061	2.663
IE	5.418	5.492	5.577
EA	1.797	2.431	2.914
μ	3.263	13.249	1.586
χ	3.608	3.962	4.246
η	1.811	1.531	1.331

The time-dependent density functional theory (TD-DFT) results are tabulated in Table S2 along with experimental values for absorption. The TD-DFT for **TP** was carried out in 100% THF, where the absorption corresponding to the 368 nm of experimental observation was confirmed to be primarily a HOMO → LUMO transition. At a lower THF concentration of 10% in the THF-aqueous solvent mixture, the absorption at higher wavelengths of 389 and 438 nm was observed to be HOMO → LUMO and HOMO → LUMO+1 excitations, shifting to the visible region from the UV region. TD-DFT calculations were carried out for the **TPZn** complex in 100% THF where absorption was experimentally observed at 395 nm. The absorption around this range was due to the indistinct charge separation between the HOMO and LUMO. Further, from 90 to 40% THF-aqueous medium, a hypsochromic shift was confirmed and the absorption was characterized by delocalized charges across the whole complex, which also supported the possibility of H-type aggregation. At 30% THF-aqueous and lower concentrations of THF in THF-aqueous medium, a bathochromic shift into the visible region was observed where the charge density shifts from **TP** to $ZnCl_2$, which supports the possibility of J-type aggregation. In the $(\mathbf{TP})_2\mathbf{Zn}$ complex, at 100% THF, the absorption was experimentally observed at 380 nm and the transitions during absorption were mostly associated with ligand-to-metal charge transfers. Further, at decreasing THF concentrations, there is a bathochromic shift, where until 40% THF-aqueous, the absorption lies within the UV range, while 30% THF-aqueous and below, the absorption occurs in the visible region. The low ΔE in $(\mathbf{TP})_2\mathbf{Zn}$ causes the transitions to be characterized with significant ligand-to-metal charge transfers along with locally excited states and intraligand charge transfer. Further, to understand the photophysical property more explicitly in terms of the bulk environment, we studied the **TPZn** monomer in its dimer form, i.e., $(\mathbf{TPZn})_2$, in different ratios of THF-aqueous solvent. The optimized geometry of $(\mathbf{TPZn})_2$ is shown in Figure S11, and the TD-DFT results are shown in Table S3. From Figure S11, it can be seen that the two **TPZn** units are in a staggered head-to-tail configuration. The TD-DFT results

https://doi.org/10.1021/acsomega.3c06283
ACS Omega 2023, 8, 48855−48872

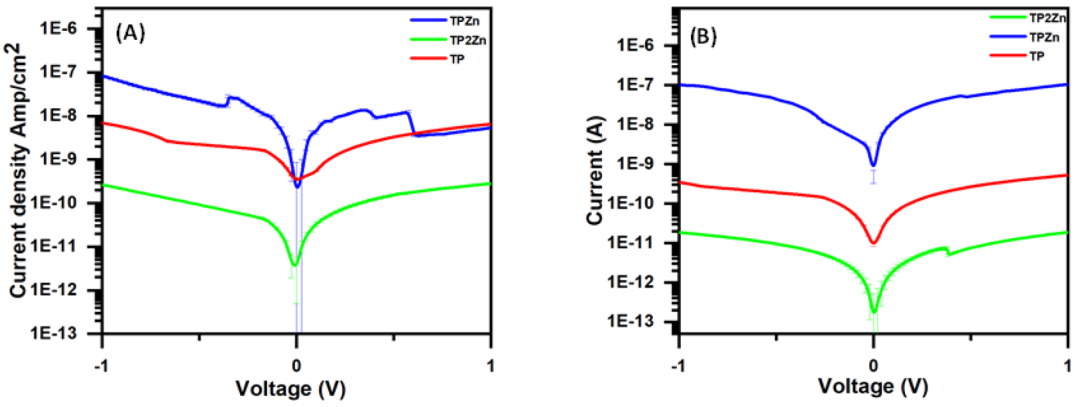

Figure 10. (A) Current density vs voltage graph (vertical measurement) for **TP**, **TPZn**, and $(\mathbf{TP})_2\mathbf{Zn}$ fabricated on ITO-coated glass surfaces and (B) current vs voltage graph (horizontal measurement) for **TP**, **TPZn**, and $(\mathbf{TP})_2\mathbf{Zn}$ fabricated on the glass substrate.

showed a slight bathochromic shift on going from a single molecule, **TPZn**, to dimer, $(\mathbf{TPZn})_2$, in the corresponding solvent polarities (i.e., 100% THF, 40% THF, and 30% THF).[75−77]

It can be expected that there should be a difference in the electronic transport efficiency across thin films of **TP** and its corresponding metal complexes (**TPZn** and $(\mathbf{TP})_2\mathbf{Zn}$) due to the difference in the energy gap originating from the frontier molecular orbitals and the associated electronic transitions. We explored the variation in electronic transport efficiency by measuring both the vertical and horizontal current−voltage correlations across thin films of **TP** and its corresponding metal complexes (**TPZn** and $(\mathbf{TP})_2\mathbf{Zn}$) of similar thickness. In horizontal measurements, we used metal electrodes on glass with a separation of 10−20 μm, and drop-casted films were prepared on it. For vertical transport, we spin-coated the films on a cleaning ITO substrate, and after solvent evaporation, we deposited Al-metal as top electrodes.

The result of area normalized $I-V$ characteristics or current density measurement analysis (both vertical and horizontal) displayed that the measured current density was higher on **TPZn**-coated surfaces, followed by **TP** and $(\mathbf{TP})_2\mathbf{Zn}$ (Figure 10A,B). Our result suggested that the measured current density was ascribed to the electron migration phenomenon, which was more pronounced on the **TPZn**-coated surface. To gain insight into the measured difference in current density for **TP**-, **TPZn**-, and $(\mathbf{TP})_2\mathbf{Zn}$-coated surfaces, we recorded the UV−vis absorption spectra of **TP**-, **TPZn**-, and $(\mathbf{TP})_2\mathbf{Zn}$-coated glass surfaces. There is a prominent redshift of the absorption maxima for all three compound-coated surfaces compared with the absorption spectra of **TP**, **TPZn**, and $(\mathbf{TP})_2\mathbf{Zn}$ in the solution phase (in THF medium) due to molecular aggregation. Utilizing the Tauc plot method,[78−80] we obtained direct band gap energies (energy difference between frontier molecular orbitals) of 3.5901 eV for **TP**, 3.3687 eV for **TPZn**, and 3.6525 eV for $(\mathbf{TP})_2\mathbf{Zn}$.

As shown in Figure S10, using the calculations, this lowest HOMO−LUMO gap in **TPZn** facilitates easier electron transport and enhances electron migration on the **TPZn**-coated glass and ITO surface. Consequently, the lowest direct band gap energy of **TPZn**, as determined by the Tauc plot method using the UV−vis absorption spectra, is attributed to the higher current and current density observed on the **TPZn**-coated glass and ITO surface, respectively, due to enhanced as well as easier electron transport. Therefore, we have improved electron migration by tuning the HOMO−LUMO gap,[81] leading to the observed order of measured current and current density, **TPZn** > **TP** > $(\mathbf{TP})_2\mathbf{Zn}$.

CONCLUSIONS

In summary, we have described the synthesis, characterization, and solvent polarity-induced optical and self-assembly properties of a functional π-conjugated molecule (**TP**) and its corresponding metal complexes (**TPZn** and $(\mathbf{TP})_2\mathbf{Zn}$). Upon changing the medium polarity, **TP**, **TPZn**, and $(\mathbf{TP})_2\mathbf{Zn}$ self-assembled into various superstructures with morphological variation and displayed aggregation-induced tunable luminescence properties. This benefits them in finding potential employment in organic electronic applications with the requirement of adjustable fluorescence output. More importantly, **TPZn** in 10% aqueous-THF medium behaves as a single-component white light emitter. DFT calculations were performed to corroborate the experimentally obtained results on the solvent polarity-induced tunable optical properties. The mechanism responsible for the morphological variation of the self-assembled structures was investigated by using various microscopic and spectroscopic techniques. Related photophysical studies and PXRD analyses suggested that the attainment of J/H-type aggregation promoted the lamellar molecular arrangement of these molecular building blocks. Furthermore, the $I-V$ characteristics of these compounds were also investigated. The electron density measurement indicated that **TPZn** demonstrated superior performance compared to **TP** and $(\mathbf{TP})_2\mathbf{Zn}$. This suggests that **TPZn** possesses better electrical conductivity or charge transport properties, which are essential for organic electronic applications. Overall, our work highlights the potential utility of phenanthro[9,10-*d*]imidazole and terpyridine-based π-conjugated probe and its corresponding Zn(II) complexes for the fabrication of diverse superstructures with tunable optical properties, which emphasizes their potential in organic electronic applications. The tunable luminescent outputs, adjustable self-assembling behavior, and superior $I-V$ characteristics of **TPZn** make this a promising material for various organic electronic applications. However, the $I-V$ characteristics of **TP**, **TPZn**, and $(\mathbf{TP})_2\mathbf{Zn}$ can help to exploit them for possible potential employment for organic field-effect transistors (OFETs) and OLED device fabrication in the future.

https://doi.org/10.1021/acsomega.3c06283
ACS Omega 2023, 8, 48855−48872

MATERIALS AND METHODS

Materials. All chemicals and solvents are commercially available and were used as received without further purification. 2-Acetylpyridine, *N*-bromosuccinimide, *p*-tolualdehyde, benzoyl peroxide, 9,10-phenanthrenequinone, potassium hydroxide, calcium carbonate, EDTA, ammonium acetate, and zinc chloride were purchased from AVRA. Ammonium hydroxide was purchased from Siscon Research Laboratories (SRL) Pvt. Ltd., India. Dichloromethane, CCl_4, 1,4-dioxane, and conc. HCl was obtained from Sigma-Aldrich. Glacial acetic acid and methanol were purchased from Finar Ltd. Other regular laboratory chemicals were purchased from Siscon Research Laboratories and Loba Chemicals (Mumbai, MH, India).

Synthesis of TP, TPZn, and $(TP)_2Zn$. The detailed procedure utilized to synthesize **TP**, **TPZn**, and $(TP)_2Zn$ is available in the Supporting Information (Schemes S1 and S2 and Figures S1−S7).

FT-IR Spectroscopy. The FT-IR spectra were recorded using an IRTracer-100 FT-IR spectrometer (Shimadzu) with a deuterated lanthanum α-alanine-doped triglycine sulfate (DLaTGS) detector. FT-IR for these synthesized **TP**, **TPZn**, and $(TP)_2Zn$ were carried out in a powder form. The measurements were taken using 4 cm^{-1} resolutions and an average of 1000 scans. The transmittance minimal values were determined using the Lab Solutions IR analysis program (IR Tracer).

Self-Assembly of TP, TPZn, and $(TP)_2Zn$. A fresh stock solution of the building blocks **TP**, **TPZn**, and $(TP)_2Zn$ was prepared by dissolving these complexes in THF to a concentration of 50 mg mL^{-1}. Then, we blended these solutions in several different solvents and diluted them to get the desired concentrations of these building blocks for self-assembly. The polarized solvent allowed the molecules to self-assemble.

High-Resolution Scanning Electron Microscopy (HR-SEM). A 10 μL drop of a self-assembled solution of **TP**, **TPZn**, and $(TP)_2Zn$ in different solvent media was placed on a glass coverslip and allowed to dry at RT. SEM analysis was performed using a high-resolution scanning electron microscope (HR-SEM, Thermo Scientific Apreo S) operating at 18 kV.

Microanalysis. (C, H, and N) analysis was carried out by using a Vario Micro Cube (Elementar) instrument for **TP**, **TPZn**, and $(TP)_2Zn$.

TGA. Thermal analysis of **TP**, **TPZn**, and $(TP)_2Zn$ was carried out using a NETZSCH NJA-STA 2500 Regulus, software Proteus, TGA thermal analyzer with a heating rate of 10 °C min^{-1} under an N_2 atmosphere.

PXRD Analysis. The PXRD pattern of the samples was recorded by using a PANalytical X'Pert Pro powder X-ray diffractometer. Data collection was carried out at room temperature using Cu K_α radiation (1.5406 Å; 40 kV, 30 mA) as the X-ray source in the 2θ continuous scan mode (Bragg−Brentano geometry) in the range of 5−50° at a scan rate of 1° min^{-1} and a time per step of 0.5 s.

UV−Vis Spectroscopy. The UV−vis absorption spectra of the synthesized metal complexes **TP**, **TPZn**, and $(TP)_2Zn$ were recorded in different solvent media with varying polarities by using a UV/vis spectrophotometer (Thermo Scientific NanoDrop 2000c UV−vis absorption spectrometer).

Fluorescence Spectroscopy. Fluorescence measurements were performed at RT using a fluorescence spectrometer (Edinburgh Instruments, FLS1000). The emission spectra of the synthesized molecules were recorded in different solvent media with varying polarities using proper excitation wavelengths.

Computational Details. The structures of **TP**, **TPZn**, and $(TP)_2Zn$ were optimized using the DFT calculations with the B3LYP functional[82,83] in the Gaussian 16 software package.[84] The GENECP basis set was used with SSD assigned to Zn in **TPZn** and $(TP)_2Zn$ and 6-31G* for all other atoms, where the B3LYP/6-31g* level of theory was employed in the optimization of **TP**.[85,86] The optimization (both the monomer and dimer) was carried out in the gas phase along with their respective frequency calculations. The absence of an imaginary frequency indicated that the optimized structures were minimal on the potential energy surface. The HOMO, LUMO, and HOMO−LUMO gap of the ligand and the Zn(II) complexes were calculated for energy at different concentrations of THF in THF-aqueous medium using the B3LYP/6-31G* level of theory with the polarized continuum model (PCM)[87] to exhibit generic solvent media (THF:water). Other electronic properties such as ionization energy (IE), electron affinity (EA), dipole moment (μ), electronegativity (χ), and global hardness (η) were calculated based on the following formulas:[88]

$$\mathrm{IE} = -E_{\mathrm{HOMO}}$$

$$\mathrm{EA} = -E_{\mathrm{LUMO}}$$

$$\chi = \frac{(\mathrm{IE} + \mathrm{EA})}{2}$$

$$\eta = \frac{(\mathrm{IE} - \mathrm{EA})}{2}$$

The optimized geometries were used to compute the absorption spectra in different polarities of the solvent (aqueous:THF) medium. The absorption values were computed with TD-DFT formalism.[89] The TD-DFT calculations were done at the B3LYP/6-31G* level of theory along with the PCM approach to simulate generic solvent (aqueous:THF) media. The limitations of the hybrid functional and the singular basis set used in the TD-DFT calculations may affect the accuracy of the absorption values.

Calculation of Direct Band Gap Energy of TP, TPZn, and $(TP)_2Zn$. At first, the direct band gap energy is determined by calculating the absorbance of **TP**, **TPZn**, and $(TP)_2Zn$ in a thin film form using a UV−vis spectrophotometer. After that, the Tauc graph plot method is applied by drawing a linear line to intersect the *X*-axis on the graph of the relationship between energy ($h\nu$) and ($\alpha h\nu$).[2,79]

$$(\alpha h\nu)^2 = A(h\nu - E_g)$$

where h is the Planck constant ($h = 6.626 \times 10^{-34}$ Js = 4.136×10^{-15} eV), ν is the beam frequency (Hz), α is the absorption coefficient, E_g is the band gap energy, and A is the energy-dependent constant.

Device Fabrication and *I*−*V* Characterization. *Horizontal I*−*V Study.* To perform the horizontal *I*−*V* measurement, we fabricated the devices on the glass surfaces. Before fabrication, these glass substrates were cleaned through sonication with deionized water, followed by soap solution,

https://doi.org/10.1021/acsomega.3c06283
ACS Omega 2023, 8, 48855−48872

acetone, and isopropanol, and dried over nitrogen gas. After that, we deposited silver contacts under a high vacuum (6×10^{-6} Torr) at a typical rate of 1−2 Å/s to create channels with a width of less than 20 μm on cleaned glass substrates using the thermal evaporation method. Finally, the investigated compound (**TP**, **TPZn**, $(\mathbf{TP})_2\mathbf{Zn}$, Conc = 5 mg mL^{-1}, in THF) solutions were drop cast on the deposited silver contacts and kept in the desiccator overnight to make the final devices ready. We measured the *I*−*V* characteristics (−1 to 1 voltage range) of these two different types of devices (glass surface and ITO surface coated with compounds) using a Keithley-2636B source measurement unit and probe station instrument.

Vertical I−*V Study*. On the other hand, for the vertical measurement, we fabricated the devices on an ITO-coated glass substrate after proper cleaning following the above-mentioned procedure. The examined compounds (5 mg mL^{-1} in THF) were drop casted onto the separate glass substrates and kept within a desiccator for solvent evaporation. To perform *I*−*V* characteristics on the fabricated device, we deposited aluminum thin film with a thickness of 50−60 nm as the cathode on top of the dried films.

■ ASSOCIATED CONTENT

Supporting Information

The Supporting Information is available free of charge at https://pubs.acs.org/doi/10.1021/acsomega.3c06283.

Synthetic methodologies adopted for the synthesis of **TP**, **TPZn**, and $(\mathbf{TP})_2\mathbf{Zn}$; ^{1}H NMR and ^{13}C NMR and TGA spectra of **TP**, **TPZn**, and $(\mathbf{TP})_2\mathbf{Zn}$; ESI mass spectra of **TP**, **TPZn**, and $(\mathbf{TP})_2\mathbf{Zn}$; temperature-dependent UV−vis spectra of **TP**, **TPZn**, and $(\mathbf{TP})_2\mathbf{Zn}$; UV−vis spectra of (A) **TP**, (B) **TPZn**, and (C) $(\mathbf{TP})_2\mathbf{Zn}$ coated at the ITO surface; Tauc plot for the band gap energy of (D) **TP**, (E) **TPZn**, and (F) $(\mathbf{TP})_2\mathbf{Zn}$; optimized geometry of $(\mathbf{TPZn})_2$; molecular orbital energy levels and their energy gaps (in eV) in **TP**, **TPZn**, and $(\mathbf{TP})_2\mathbf{Zn}$; calculated absorption of **TP**, **TPZn**, and $(\mathbf{TP})_2\mathbf{Zn}$ in different aqueous:THF ratios at the TD-B3LYP/6-31g* level of theory along with the experimental values; calculated absorption of $(\mathbf{TPZn})_2$ in different aqueous:THF ratios at the TD-B3LYP/6-31g* level of theory along with the experimental values (PDF)

■ AUTHOR INFORMATION

Corresponding Authors

Elumalai Varathan − *Department of Chemistry, SRM Institute of Science and Technology, Kattankulathur, Tamil Nadu 603203, India;* orcid.org/0000-0003-4331-9460; Email: varathan.elumalai85@gmail.com, varathae@srmist.edu.in

Priyadip Das − *Department of Chemistry, SRM Institute of Science and Technology, Kattankulathur, Tamil Nadu 603203, India;* orcid.org/0000-0001-5924-6660; Email: priyadipcsmcri@gmail.com, priyadip@srmist.edu.in

Authors

Priya Rana − *Department of Chemistry, SRM Institute of Science and Technology, Kattankulathur, Tamil Nadu 603203, India*

Abigail Jennifer G − *Department of Chemistry, SRM Institute of Science and Technology, Kattankulathur, Tamil Nadu 603203, India;* orcid.org/0000-0002-5809-1916

Shanmuka Rao T − *Department of Physics, SRM University, Guntur, Andhra Pradesh 522240, India*

Sabyasachi Mukhopadhyay − *Department of Physics, SRM University, Guntur, Andhra Pradesh 522240, India;* orcid.org/0000-0002-6290-6380

Complete contact information is available at: https://pubs.acs.org/10.1021/acsomega.3c06283

Author Contributions

Conceptualization and design, P.D. and E.V.; acquisition of data, P.R., A.J.G., and S.R.T.; analysis and interpretation of data, P.R., A.J.G., S.R.T., S.M., E.V., and P.D.; writing or revision of the manuscript, P.R., A.J.G., S.M., E.V., and P.D.; study supervision, E.V. and P.D.

Notes

The authors declare no competing financial interest.

■ ACKNOWLEDGMENTS

P.D. acknowledges the Council of Scientific and Industrial Research (CSIR) (file no. 01(3077)/21/EMR-II) for research funding and the support of the Interdisciplinary Institute of Indian System of Medicine (IIISM) for providing NMR and ESI mass spectrometry facility, Nano Research Centre (NRC), and Department of Chemistry of SRM IST for several characterization studies. S.M. acknowledges the Science and Engineering Research Board (DST, GOI) for ECR/2017/001937 fund and SRM University Andhra Pradesh for seed research grants. E.V. expresses his gratitude to the Department of Science and Technology (DST), Government of India's Science and Engineering Research Board (SERB), for awarding the Start-up Research Grant (SERB-SRG) with reference number SRG/2022/000207. E.V and A.J.G. acknowledge the High-Performance Computing Center, SRM Institute of Science and Technology for providing the computational facility.

■ REFERENCES

(1) Palmer, L. C.; Stupp, S. I. Molecular Self-Assembly into One-Dimensional Nanostructures. *Acc. Chem. Res.* **2008**, *41* (12), 1674−1684.

(2) Ajayaghosh, A.; Praveen, V. K. π-Organogels of Self-Assembled p-Phenylenevinylenes: Soft Materials with Distinct Size, Shape, and Functions. *Acc. Chem. Res.* **2007**, *40* (8), 644−656.

(3) Gröschel, A. H.; Müller, A. H. E. Self-Assembly Concepts for Multicompartment Nanostructures. *Nanoscale* **2015**, *7* (28), 11841−11876.

(4) Lim, Y.; Moon, K. S.; Lee, M. Recent Advances in Functional Supramolecular Nanostructures Assembled from Bioactive Building Blocks. *Chem. Soc. Rev.* **2009**, *38* (4), 925−934.

(5) Haedler, A. T.; Kreger, K.; Issac, A.; Wittmann, B.; Kivala, M.; Hammer, N.; Köhler, J.; Schmidt, H.-W.; Hildner, R. Long-Range Energy Transport in Single Supramolecular Nanofibres at Room Temperature. *Nature* **2015**, *523* (7559), 196−199.

(6) Misra, R.; Reja, R. M.; Narendra, L. V.; George, G.; Raghothama, S.; Gopi, H. N. Exploring Structural Features of Folded Peptide Architectures in the Construction of Nanomaterials. *Chem. Commun.* **2016**, *52* (61), 9597−9600.

(7) Ishikawa, K.; Kameta, N.; Aoyagi, M.; Asakawa, M.; Shimizu, T. Soft Nanotubes with a Hydrophobic Channel Hybridized with Au Nanoparticles: Photothermal Dispersion/Aggregation Control of C60 in Water. *Adv. Funct. Mater.* **2013**, *23* (13), 1677−1683.

(8) Ghosh, S.; Philips, D. S.; Saeki, A.; Ajayaghosh, A. Nanosheets of an Organic Molecular Assembly from Aqueous Medium Exhibit High Solid-State Emission and Anisotropic Charge-Carrier Mobility. *Adv. Mater.* **2017**, *29* (10), 1605408.
(9) Yan, X.; Zhu, P.; Li, J. Self-Assembly and Application of Diphenylalanine-Based Nanostructures. *Chem. Soc. Rev.* **2010**, *39* (6), 1877−1890.
(10) Tian, Y.; Li, J.; Zhao, L.; Zhang, X.; Wang, A.; Jian, H.; Bai, S.; Yan, X. Peptide Assembly Assisted Triplet−Triplet Annihilation Photon Upconversion in Non-Deoxygenated Water. *Biomater. Sci.* **2020**, *8* (11), 3072−3077.
(11) Hoeben, F. J. M.; Jonkheijm, P.; Meijer, E. W.; Schenning, A. P. H. J. About Supramolecular Assemblies of π-Conjugated Systems. *Chem. Rev.* **2005**, *105* (4), 1491−1546.
(12) Rana, P.; Marappan, G.; Sivagnanam, S.; Surya, V. J.; Sivalingam, Y.; Das, P. Self-Assembly Induced Tunable Multiple Fluorescence Output from a White Light-Emitting Functionalized Single π-Conjugated Molecule and Implication in VOC Sensing Applications. *Mater. Chem. Front.* **2022**, *6* (11), 1421−1436.
(13) Zang, L.; Che, Y.; Moore, J. S. One-Dimensional Self-Assembly of Planar π-Conjugated Molecules: Adaptable Building Blocks for Organic Nanodevices. *Acc. Chem. Res.* **2008**, *41* (12), 1596−1608.
(14) Sun, B.; Tao, K.; Jia, Y.; Yan, X.; Zou, Q.; Gazit, E.; Li, J. Photoactive Properties of Supramolecular Assembled Short Peptides. *Chem. Soc. Rev.* **2019**, *48* (16), 4387−4400.
(15) Ghosh, A.; Shrivastav, A.; Jose, D. A.; Mishra, S. K.; Chandrakanth, C. K.; Mishra, S.; Das, A. Colorimetric Sensor for Triphosphates and Their Application as a Viable Staining Agent for Prokaryotes and Eukaryotes. *Anal. Chem.* **2008**, *80* (14), 5312−5319.
(16) Mahato, P.; Ghosh, A.; Mishra, S. K.; Shrivastav, A.; Mishra, S.; Das, A. Zn(II) Based Colorimetric Sensor for ATP and Its Use as a Viable Staining Agent in Pure Aqueous Media of PH 7.2. *Chem. Commun.* **2010**, *46* (48), 9134−9136.
(17) Li, Y.; Liu, T.; Liu, H.; Tian, M. Z.; Li, Y. Self-Assembly of Intramolecular Charge-Transfer Compounds into Functional Molecular Systems. *Acc. Chem. Res.* **2014**, *47* (4), 1186−1198.
(18) Yang, D.; Gao, S.; Fang, Y.; Lin, X.; Jin, X.; Wang, X.; Ke, L.; Shi, K. The π−π Stacking-Guided Supramolecular Self-Assembly of Nanomedicine for Effective Delivery of Antineoplastic Therapies. *Nanomedicine* **2018**, *13* (24), 3159−3177.
(19) Maity, A.; Ali, F.; Agarwalla, H.; Anothumakkool, B.; Das, A. Tuning of Multiple Luminescence Outputs and White-Light Emission from a Single Gelator Molecule through an ESIPT Coupled AIEE Process. *Chem. Commun.* **2015**, *51* (11), 2130−2133.
(20) Singha Mahapatra, T.; Singh, H.; Maity, A.; Dey, A.; Pramanik, S. K.; Suresh, E.; Das, A. White-Light-Emitting Lanthanide and Lanthanide-Iridium Doped Supramolecular Gels: Modular Luminescence and Stimuli-Responsive Behaviour. *J. Mater. Chem. C* **2018**, *6* (36), 9756−9766.
(21) Li, G.; Wu, Y.; Gao, J.; Wang, C.; Li, J.; Zhang, H.; Zhao, Y.; Zhao, Y.; Zhang, Q. Synthesis and Physical Properties of Four Hexazapentacene Derivatives. *J. Am. Chem. Soc.* **2012**, *134* (50), 20298−20301.
(22) Zou, Q.; Liu, K.; Abbas, M.; Yan, X. Peptide-Modulated Self-Assembly of Chromophores toward Biomimetic Light-Harvesting Nanoarchitectonics. *Adv. Mater.* **2016**, *28* (6), 1031−1043.
(23) Agarwalla, H.; Pal, S.; Paul, A.; Jun, Y. W.; Bae, J.; Ahn, K. H.; Srivastava, D. N.; Das, A. A Fluorescent Probe for Bisulfite Ions: Its Application to Two-Photon Tissue Imaging. *J. Mater. Chem. B* **2016**, *4* (48), 7888−7894.
(24) Das, P.; Bhattacharya, S.; Mishra, S.; Das, A. Zn(Ii) and Cd(Ii)-Based Complexes for Probing the Enzymatic Hydrolysis of Na4P2O7 by Alkaline Phosphatase in Physiological Conditions. *Chem. Commun.* **2011**, *47* (28), 8118−8120.
(25) Dimitrakopoulos, C. D.; Malenfant, P. R. L. Organic Thin Film Transistors for Large Area Electronics. *Adv. Mater.* **2002**, *14* (2), 99−117.
(26) Braun, D. Semiconducting Polymer LEDs. *Mater. Today* **2002**, *5* (6), 32−39.
(27) Friend, R. H.; Gymer, R. W.; Holmes, A. B.; Burroughes, J. H.; Marks, R. N.; Taliani, C.; Bradley, D. D. C.; Dos Santos, D. A.; Brédas, J. L.; Lögdlund, M.; Salaneck, W. R. Electroluminescence in Conjugated Polymers. *Nature* **1999**, *397* (6715), 121−128.
(28) Brabec, C. J.; Dyakonov, V.; Parisi, J.; Sariciftci, N. S. *Organic Photovoltaics*; Brabec, C. J.; Dyakonov, V.; Parisi, J.; Sariciftci, N. S., Eds.; Springer Series in Materials Science; Springer Berlin Heidelberg: Berlin, Heidelberg, 2003; Vol. *60*. DOI: 10.1007/978-3-662-05187-0.
(29) Ashoka, A. H.; Ali, F.; Tiwari, R.; Kumari, R.; Pramanik, S. K.; Das, A. Recent Advances in Fluorescent Probes for Detection of HOCl and HNO. *ACS Omega* **2020**, *5* (4), 1730−1742.
(30) Zhao, L.; Ren, X.; Yan, X. Assembly Induced Super-Large Red-Shifted Absorption: The Burgeoning Field of Organic Near-Infrared Materials. *CCS Chem.* **2021**, *3* (5), 678−693.
(31) Agarwalla, H.; Mahajan, P. S.; Sahu, D.; Taye, N.; Ganguly, B.; Mhaske, S. B.; Chattopadhyay, S.; Das, A. A Switch-On NIR Probe for Specific Detection of Hg 2+ Ion in Aqueous Medium and in Mitochondria. *Inorg. Chem.* **2016**, *55* (22), 12052−12060.
(32) Ren, X.; Zou, Q.; Yuan, C.; Chang, R.; Xing, R.; Yan, X. The Dominant Role of Oxygen in Modulating the Chemical Evolution Pathways of Tyrosine in Peptides: Dityrosine or Melanin. *Angew. Chemie Int. Ed.* **2019**, *58* (18), 5872−5876.
(33) Zou, R.; Wang, Q.; Wu, J.; Wu, J.; Schmuck, C.; Tian, H. Peptide Self-Assembly Triggered by Metal Ions. *Chem. Soc. Rev.* **2015**, *44* (15), 5200−5219.
(34) Krebs, A.; Ludwig, V.; Pfizer, J.; Dürner, G.; Göbel, M. W. Enantioselective Synthesis of Non-Natural Aromatic α-Amino Acids. *Chem. - Eur. J.* **2004**, *10* (2), 544−553.
(35) Zuend, S. J.; Coughlin, M. P.; Lalonde, M. P.; Jacobsen, E. N. Scaleable Catalytic Asymmetric Strecker Syntheses of Unnatural α-Amino Acids. *Nature* **2009**, *461* (7266), 968−970.
(36) Das, P.; Pan, I.; Cohen, E.; Reches, M. Self-Assembly of a Metallo-Peptide into a Drug Delivery System Using a "Switch on" Displacement Strategy. *J. Mater. Chem. B* **2018**, *6* (48), 8228−8237.
(37) Kula, S.; Szlapa-Kula, A.; Kotowicz, S.; Filapek, M.; Bujak, K.; Siwy, M.; Janeczek, H.; Maćkowski, S.; Schab-Balcerzak, E. Phenanthro[9,10-d]Imidazole with Thiophene Rings toward OLEDs Application. *Dye. Pigment.* **2018**, *159*, 646−654.
(38) Dias, G. G.; Rodrigues, M. O.; Paz, E. R. S.; Nunes, M. P.; Araujo, M. H.; Rodembusch, F. S.; da Silva Júnior, E. N. Aryl-Phenanthro[9,10-d]Imidazole: A Versatile Scaffold for the Design of Optical-Based Sensors. *ACS Sens.* **2022**, *7* (10), 2865−2919.
(39) Idris, M.; Coburn, C.; Fleetham, T.; Milam-Guerrero, J.; Djurovich, P. I.; Forrest, S. R.; Thompson, M. E. Phenanthro[9,10- d] Triazole and Imidazole Derivatives: High Triplet Energy Host Materials for Blue Phosphorescent Organic Light Emitting Devices. *Mater. Horizons* **2019**, *6* (6), 1179−1186.
(40) Das, P.; Ghosh, A.; Kesharwani, M. K.; Ramu, V.; Ganguly, B.; Das, A. Zn II − 2,2′:6′,2″-Terpyridine-Based Complex as Fluorescent Chemosensor for PPi, AMP and ADP. *Eur. J. Inorg. Chem.* **2011**, *2011* (20), 3050−3058.
(41) Constable, E. C. 2,2′:6′,2″-Terpyridines: From Chemical Obscurity to Common Supramolecular Motifs. *Chem. Soc. Rev.* **2007**, *36* (2), 246−253.
(42) Wild, A.; Winter, A.; Schlütter, F.; Schubert, U. S. Advances in the Field of π-Conjugated 2,2′:6′,2″-Terpyridines. *Chem. Soc. Rev.* **2011**, *40* (3), 1459−1511.
(43) Schultz, A.; Cao, Y.; Huang, M.; Cheng, S. Z. D.; Li, X.; Moorefield, C. N.; Wesdemiotis, C.; Newkome, G. R. Stable, Trinuclear Zn(Ii)- and Cd(Ii)-Metallocycles: TWIM-MS, Photophysical Properties, and Nanofiber Formation. *Dalt. Trans.* **2012**, *41* (38), 11573−11575.
(44) Cui, B. B.; Shao, J. Y.; Zhong, Y. W. Bis-Tridentate Ruthenium Complexes with a Redox-Active Amine Substituent: Electrochemical, Spectroscopic, and DFT/TDDFT Studies. *Organometallics* **2014**, *33* (16), 4220−4229.
(45) Nie, H. J.; Yao, C. J.; Sun, M. J.; Zhong, Y. W.; Yao, J. Ruthenium- Bis -Terpyridine Complex with Two Redox-Asymmetric

https://doi.org/10.1021/acsomega.3c06283
ACS Omega 2023, 8, 48855−48872

Amine Substituents: Potential-Controlled Reversal of the Direction of Charge-Transfer. *Organometallics* **2014**, *33* (21), 6223−6231.
(46) Wu, K. Q.; Guo, J.; Yan, J. F.; Xie, L.; Xu, F. B.; Bai, S.; Nockemann, P.; Yuan, Y.-F. Alkynyl-Bridged Ruthenium(II) 4′-Diferrocenyl-2,2′:6′,2″-Terpyridine Electron Transfer Complexes: Synthesis, Structures, and Electrochemical and Spectroscopic Studies. *Organometallics* **2011**, *30* (13), 3504−3511.
(47) Yao, C. J.; Yao, J.; Zhong, Y. W. Electronic Communication between Two Amine Redox Centers Bridged by a Bis(Terpyridine)-Ruthenium(II) Complex. *Inorg. Chem.* **2011**, *50* (15), 6847−6849.
(48) Winter, A.; Newkome, G. R.; Schubert, U. S. Catalytic Applications of Terpyridines and Their Transition Metal Complexes. *ChemCatChem.* **2011**, *3* (9), 1384−1406.
(49) Ghasemi, E.; Alimardani, E.; Shams, E.; Koohmareh, G. A. Modification of Glassy Carbon Electrode with Iron-Terpyridine Complex and Iron-Terpyridine Complex Covalently Bonded to Ordered Mesoporous Carbon Substrate: Preparation, Electrochemistry and Application to H_2O_2 Determination. *J. Electroanal. Chem.* **2017**, *789*, 92−99.
(50) Muller, R. S.; Kamins, T. I. *Device Electronics for Integrated Circuits*; 1986.
(51) Lee, J. K.; Yang, M. Progress in Light Harvesting and Charge Injection of Dye-Sensitized Solar Cells. *Mater. Sci. Eng., B* **2011**, *176* (15), 1142−1160.
(52) Wang, Z.; Wang, F.; Sun, W.; Ni, R.; Hu, S.; Liu, J.; Zhang, B.; Alsaed, A.; Hayat, T.; Tan, Z. Manipulating the Trade-off Between Quantum Yield and Electrical Conductivity for High-Brightness Quasi-2D Perovskite Light-Emitting Diodes. *Adv. Funct. Mater.* **2018**, *28* (47), 1804187.
(53) Yoon, E.; Jang, K. Y.; Park, J.; Lee, T. Understanding the Synergistic Effect of Device Architecture Design toward Efficient Perovskite Light-Emitting Diodes Using Interfacial Layer Engineering. *Adv. Mater. Interfaces* **2021**, *8* (3), 2001712.
(54) Maity, A.; Dey, A.; Gangopadhyay, M.; Das, A. Water Induced Morphological Transformation of a Poly(Aryl Ether) Dendron Amphiphile: Helical Fibers to Nanorods, as Light-Harvesting Antenna Systems. *Nanoscale* **2018**, *10* (3), 1464−1473.
(55) Wang, J.; Yuan, C.; Han, Y.; Wang, Y.; Liu, X.; Zhang, S.; Yan, X. Trace Water as Prominent Factor to Induce Peptide Self-Assembly: Dynamic Evolution and Governing Interactions in Ionic Liquids. *Small* **2017**, *13* (44), 1702175.
(56) Liu, Y.; Naumenko, E.; Akhatova, F.; Zou, Q.; Fakhrullin, R.; Yan, X. Self-Assembled Peptide Nanoparticles for Enhanced Dark-Field Hyperspectral Imaging at the Cellular and Invertebrate Level. *Chem. Eng. J.* **2021**, *424*, No. 130348.
(57) Sivagnanam, S.; Basak, M.; Kumar, A.; Das, K.; Mahata, T.; Rana, P.; Sengar, A. S.; Ghosh, S.; Subramanian, M.; Stewart, A.; Maity, B.; Das, P. Supramolecular Structures Generated via Self-Assembly of a Cell Penetrating Tetrapeptide Facilitate Intracellular Delivery of a Pro-Apoptotic Chemotherapeutic Drug. *ACS Appl. Bio Mater.* **2021**, *4* (9), 6807−6820.
(58) Kasha, M. Energy Transfer Mechanisms and the Molecular Exciton Model for Molecular Aggregates1,2. *Radiat. Res.* **2012**, *178* (2), AV27−AV34.
(59) Más-Montoya, M.; Janssen, R. A. J. The Effect of H- and J-Aggregation on the Photophysical and Photovoltaic Properties of Small Thiophene-Pyridine-DPP Molecules for Bulk-Heterojunction Solar Cells. *Adv. Funct. Mater.* **2017**, *27* (16), 1605779.
(60) Hong, J.; Jeon, S.; Kim, J. J.; Devi, D.; Chacon-Madrid, K.; Lee, W.; Koo, S. M.; Wildeman, J.; Sfeir, M. Y.; Peteanu, L. A.; Wen, J.; Ma, J. The Effects of Side-Chain-Induced Disorder on the Emission Spectra and Quantum Yields of Oligothiophene Nanoaggregates: A Combined Experimental and MD-TDDFT Study. *J. Phys. Chem. A* **2014**, *118* (45), 10464−10473.
(61) Li, S.; Chang, R.; Zhao, L.; Xing, R.; van Hest, J. C. M.; Yan, X. Two-Photon Nanoprobes Based on Bioorganic Nanoarchitectonics with a Photo-Oxidation Enhanced Emission Mechanism. *Nat. Commun.* **2023**, *14* (1), 5227.
(62) Anantharaman, S. B.; Kohlbrecher, J.; Rainò, G.; Yakunin, S.; Stöferle, T.; Patel, J.; Kovalenko, M.; Mahrt, R. F.; Nüesch, F. A.; Heier, J. Enhanced Room-Temperature Photoluminescence Quantum Yield in Morphology Controlled J-Aggregates. *Adv. Sci.* **2021**, *8* (4), 1903080.
(63) Maiti, N. C.; Mazumdar, S.; Periasamy, N. J- and H-Aggregates of Porphyrin−Surfactant Complexes: Time-Resolved Fluorescence and Other Spectroscopic Studies. *J. Phys. Chem. B* **1998**, *102* (9), 1528−1538.
(64) Belletête, M.; Bouchard, J.; Leclerc, M.; Durocher, G. Photophysics and Solvent-Induced Aggregation of 2,7-Carbazole-Based Conjugated Polymers. *Macromolecules* **2005**, *38* (3), 880−887.
(65) Yuan, W. Z.; Lu, P.; Chen, S.; Lam, J. W. Y.; Wang, Z.; Liu, Y.; Kwok, H. S.; Ma, Y.; Tang, B. Z. Changing the Behavior of Chromophores from Aggregation-Caused Quenching to Aggregation-Induced Emission: Development of Highly Efficient Light Emitters in the Solid State. *Adv. Mater.* **2010**, *22* (19), 2159−2163.
(66) Qin, L.; Lv, K.; Shen, Z.; Liu, M. Self-Assembly of Organic Molecules into Nanostructures. In *Soft Matter Nanotechnology*; Wiley-VCH Verlag GmbH & Co. KGaA: Weinheim, Germany, 2015; pp 21−94. DOI: 10.1002/9783527682157.ch02.
(67) Yuan, C.; Xing, R.; Cui, J.; Fan, W.; Li, J.; Yan, X. Multistep Desolvation as a Fundamental Principle Governing Peptide Self-Assembly Through Liquid−Liquid Phase Separation. *CCS Chem.* **2023**, 1−11.
(68) Xing, R.; Yuan, C.; Fan, W.; Ren, X.; Yan, X. Biomolecular Glass with Amino Acid and Peptide Nanoarchitectonics. *Sci. Adv.* **2023**, *9* (11), No. eadd8105, DOI: 10.1126/sciadv.add8105.
(69) Chang, H. Y.; Wu, K. Y.; Chen, W. C.; Weng, J. T.; Chen, C. Y.; Raj, A.; Hamaguchi, H.; Chuang, W.-T.; Wang, X.; Wang, C.-L. Water-Induced Self-Assembly of Amphiphilic Discotic Molecules for Adaptive Artificial Water Channels. *ACS Nano* **2021**, *15* (9), 14885−14890.
(70) Hafizovic, J.; Bjørgen, M.; Olsbye, U.; Dietzel, P. D. C.; Bordiga, S.; Prestipino, C.; Lamberti, C.; Lillerud, K. P. The Inconsistency in Adsorption Properties and Powder XRD Data of MOF-5 Is Rationalized by Framework Interpenetration and the Presence of Organic and Inorganic Species in the Nanocavities. *J. Am. Chem. Soc.* **2007**, *129* (12), 3612−3620.
(71) Samanta, S. K.; Bhattacharya, S. Aggregation Induced Emission Switching and Electrical Properties of Chain Length Dependent π-Gels Derived from Phenylenedivinylene Bis-Pyridinium Salts in Alcohol−Water Mixtures. *J. Mater. Chem.* **2012**, *22* (48), 25277−25287.
(72) Arul, A.; Rana, P.; Das, K.; Pan, I.; Mandal, D.; Stewart, A.; Maity, B.; Ghosh, S.; Das, P. Fabrication of Self-Assembled Nanostructures for Intracellular Drug Delivery from Diphenylalanine Analogues with Rigid or Flexible Chemical Linkers. *Nanoscale Adv.* **2021**, *3* (21), 6176−6190.
(73) Mandal, D.; Dinda, S.; Choudhury, P.; Das, P. K. Solvent Induced Morphological Evolution of Cholesterol Based Glucose Tailored Amphiphiles: Transformation from Vesicles to Nanoribbons. *Langmuir* **2016**, *32* (38), 9780−9789.
(74) Ungureanu, E. M.; Tatu, M. L.; Georgescu, E.; Boscornea, C.; Popa, M. M.; Stanciu, G. Influence of the Chemical Structure and Solvent Polarity on the Fluorescence of 3-Aryl-7-Benzoyl-Pyrrolo [1,2-c]Pyrimidines. *Dye. Pigment.* **2020**, *174*, No. 108023.
(75) Temerova, D.; Kisel, K. S.; Eskelinen, T.; Melnikov, A. S.; Kinnunen, N.; Hirva, P.; Shakirova, J. R.; Tunik, S. P.; Grachova, E. V.; Koshevoy, I. O. Diversifying the Luminescence of Phenanthro-Diimine Ligands in Zinc Complexes. *Inorg. Chem. Front.* **2021**, *8* (10), 2549−2560.
(76) Nie, F.; Wang, K. Z.; Yan, D. Supramolecular Glasses with Color-Tunable Circularly Polarized Afterglow through Evaporation-Induced Self-Assembly of Chiral Metal−Organic Complexes. *Nat. Commun.* **2023**, *14* (1), 1654.
(77) Salassa, G.; Castilla, A. M.; Kleij, A. W. Cooperative Self-Assembly of a Macrocyclic Schiff Base Complex. *Dalt. Trans.* **2011**, *40* (19), 5236−5243.

(78) Aderne, R. E.; Borges, B. G. A. L.; Ávila, H. C.; von Kieseritzky, F.; Hellberg, J.; Koehler, M.; Cremona, M.; Roman, L. S.; Araujo, C. M.; Rocco, M. L. M.; Marchiori, C. F. N. On the Energy Gap Determination of Organic Optoelectronic Materials: The Case of Porphyrin Derivatives. *Mater. Adv.* **2022**, *3* (3), 1791−1803.
(79) Uddin, M. N.; Islam, R.; Rahman, M.; Chawdhury, N. Comparative Photovoltaics of P3HT:N2200 and P3HT: Small-Gap Fullerene Ethyl-Nipecotate Bulk Heterojunction Structures. *Makara J. Sci.* **2022**, *26* (3), 200−208.
(80) AL-Hammadi, A. H.; Khoreem, S. H. Investigations on Optical and Electrical Conductivity of Ba/Ni/Zn/Fe16O27 Ferrite Nanoparticles. *Biointerface Res. Appl. Chem.* **2022**, *13* (2), 168.
(81) Harikrishnan, M.; Sadhasivam, V.; Siva, A.; Anandan, S.; Subbiah, V.; Murugesan, S. Energy Level Tuning of Novel Star-Shaped D−π−D−A-Based Metal-Free Organic Dyes for Solar Cell Application. *J. Phys. Chem. C* **2019**, *123* (36), 21959−21968.
(82) Miehlich, B.; Savin, A.; Stoll, H.; Preuss, H. Results Obtained with the Correlation Energy Density Functionals of Becke and Lee, Yang and Parr. *Chem. Phys. Lett.* **1989**, *157* (3), 200−206.
(83) Becke, A. D. Density-Functional Exchange-Energy Approximation with Correct Asymptotic Behavior. *Phys. Rev. A* **1988**, *38* (6), 3098−3100.
(84) Frisch, M. J., Trucks, G. W.; Schlegel, H. B.; Scuseria, G. E.; Robb, M. a.; Cheeseman, J. R.; Scalmani, G.; Barone, V.; Petersson, G. a.; Nakatsuji, H.; Li, X.; Caricato, M.; Marenich, a. V.; Bloino, J.; Janesko, B. G.; Gomperts, R.; Mennucci, B.; Hratch, D. J. *Gaussian 16, Revision C.01*; 2016.
(85) VandeVondele, J.; Hutter, J. Gaussian Basis Sets for Accurate Calculations on Molecular Systems in Gas and Condensed Phases. *J. Chem. Phys.* **2007**, *127* (11), 114105.
(86) VandeVondele, J.; Krack, M.; Mohamed, F.; Parrinello, M.; Chassaing, T.; Hutter, J. Quickstep: Fast and Accurate Density Functional Calculations Using a Mixed Gaussian and Plane Waves Approach. *Comput. Phys. Commun.* **2005**, *167* (2), 103−128.
(87) Cancès, E.; Mennucci, B.; Tomasi, J. A New Integral Equation Formalism for the Polarizable Continuum Model: Theoretical Background and Applications to Isotropic and Anisotropic Dielectrics. *J. Chem. Phys.* **1997**, *107* (8), 3032−3041.
(88) Shaikh, A. M.; Sharma, B. K.; Chacko, S.; Kamble, R. M. Synthesis and Optoelectronic Investigations of Triarylamines Based on Naphtho[2,3-f]Quinoxaline-7,12-Dione Core as Donor−Acceptors for n-Type Materials. *RSC Adv.* **2016**, *6* (65), 60084−60093.
(89) Nkungli, N. K.; Ghogomu, J. N.; Nogheu, L. N.; Gadre, S. R. DFT and TD-DFT Study of Bis[2-(5-Amino-[1,3,4]-Oxadiazol-2-Yl) Phenol](Diaqua)M(II) Complexes [M = Cu, Ni and Zn]: Electronic Structures, Properties and Analyses. *Comput. Chem.* **2015**, *03* (03), 29−44.

https://doi.org/10.1021/acsomega.3c06283
ACS Omega 2023, 8, 48855−48872